

Article

Seasonal Variability of Wind Sea and Swell Waves Climate along the Canary Current: The Local Wind Effect

Alvaro Semedo ^{1,2}

¹ Department of Water Science and Engineering, IHE Delft, P.O. Box 3015, 2601 DA Delft, The Netherlands; a.semedo@un-ihe.org

² Instituto Dom Luiz, University of Lisbon, Campo Grande, 1749-016 Lisbon, Portugal

Received: 12 December 2017; Accepted: 13 March 2018; Published: 20 March 2018

Abstract: A climatology of wind sea and swell waves along the Canary eastern boundary current area, from west Iberia to Mauritania, is presented. The study is based on the European Centre for Medium-Range Weather Forecasts (ECMWF) reanalysis ERA-Interim. The wind regime along the Canary Current, along west Iberia and north-west Africa, varies significantly from winter to summer. High summer wind speeds generate high wind sea waves, particularly along the coasts of Morocco and Western Sahara. Lower winter wind speeds, along with stronger extratropical storms crossing the North Atlantic sub-basin up north lead to a predominance of swell waves in the area during from December to February. In summer, the coast parallel wind interacts with the coastal headlands, increasing the wind speed and the locally generated waves. The spatial patterns of the wind sea or swell regional wave fields are shown to be different from the open ocean, due to coastal geometry, fetch dimensions, and island sheltering.

Keywords: wind sea; swell; coastal winds; west Iberia; north-west Africa; wave climate

1. Introduction

Two types of wind-generated gravity waves (henceforth simply called “waves”) coexist at the ocean surface: wind sea and swell. Wind seas are waves under growing process receiving energy from the overlaying wind, and strongly coupled to the local wind field. Waves that propagate away from their generation area and no longer receive energy input from the local wind are called swell. Swell waves can travel long distances across the ocean, up to 20,000 km, half of the Earth’s perimeter [1–4]. Since swells can propagate such long distances, the wave field is, most of the times, the result of contributions from waves with different frequencies (periods) and incoming directions: wind seas, and young and old swell waves, reflecting different origins and ages. For this reason, the wave field, particularly in the open ocean, does not necessarily reflect the local wind-field characteristics [5–8].

Recent studies have devoted their attention to the qualitative analysis of the wave field, from a wave-climate perspective [5–12] to an air-sea interaction point of view [13–18]. The reason for this lies mostly in the fact that the air–sea exchanging and interaction processes are sea-state dependent, i.e., the way waves modulate the exchange of momentum, heat, mass, and several other scalars across the air-sea interface is influenced by the prevalence of one type of waves over the other [19,20]. For example, as swell waves propagate into light wind areas they perform work on the overlying atmosphere, inducing a pressure perturbation in the first few meters of the marine atmospheric boundary layer (MABL), producing a forward thrust on the flow [14,17,21,22]. Swell loses energy to the atmosphere as it gradually decays [2,23], accelerating the airflow at lower altitudes, in the form of the so called “wave-driven wind”, inducing a departure from the logarithmic wind

profile [15,21]. For this reason swell has a consistent influence on the overall turbulence structure of the boundary layer, since it reduces the wind shear in the MABL and consequently the mechanical production of turbulence [14,15,18,22,23]. Under the wave-growing process, energy is transferred to the ocean throughout vertical transport of horizontal momentum via momentum flux, which drives currents, generates waves, and triggers wave breaking. Waves also induce currents at the ocean surface (the Stokes Drift; [24]) that are mostly driven by wind sea waves [12,25]. The Stokes drift velocity and the mass transport is highest along the extratropical areas, and in some regional areas along equator-ward eastern boundary currents (EBC), where the wave induced turbulence in the ocean surface boundary layer (OSBL) is also highest [26]. The wave breaking and white-capping, enhance the turbulence in the OSBL, drive mass and gas transfer between the ocean and the lower atmosphere [19,27] and change the ocean surface albedo [28,29].

From a wave-climate point of view, the need for a qualitative analysis of the wave-field characteristics lies in the fact that the most common parameters used to characterize it, the significant wave height (SWH) and the mean wave period (MWP), provide limited description of the sea-state. These two parameters are statistical integrated parameters, computed from the wave spectra, and two wave fields with the same SWH and MWP may still be different in detail, since they can be more or less dominated by one type of waves [7,30]). Hence a more detailed investigation is needed to correctly define the wave-field characteristics and the wave. The way to pursue this analysis is by studying the wind sea and swell wave parameters separately, through the partition of the wave spectra into wind sea (high frequency) and swell (low frequency) parts [31–34]. Wave-spectra observations are available mostly from in situ buoy measurements, which can only be found in coastal areas. Their very sparse geographical distribution does not allow the use of buoy data for wave-climate studies in large areas. Remote-sensing wave measurements could be an alternative to wave buoys, since they provide global coverage. Nevertheless the use of remote-sensing wave observations, for wave climate studies, is still restricted to altimeter sensors, which only provide SWH [35]. Synthetic aperture radar (SAR) sensors are the only remote-sensing instruments capable of measuring wave spectra, but the retrieval of wave spectra from SAR images still entails problems that limit its full operational use [36]. Wave reanalysis or hindcasts offer a good and sufficiently long alternative to these limitations, despite some problems, like the lack of homogeneity due to observations still present [37,38].

The wind field in the eastern flanks of the semi-permanent subtropical high pressure systems, along the EBC systems, is highly seasonal. During winter westerly winds are more prevalent, particularly in the northern hemisphere [39,40]. During summer thermal low pressure systems develop over land, and persistent equator-ward coastal wind develops. The resulting coast parallel summer winds are the geostrophically adjusted response to this synoptic pattern that drives upwelling along the mid-latitude west coasts, due to Ekman transport offshore, bringing deep cold water to the shelf and to the surface [41]. The low sea-surface temperature (SST) at the coast, in turn, sharpens the temperature and pressure gradients there, leading to a local increase of the wind speed along the coast, giving rise to the occurrence of coastal low-level jets (CLLJ) [41,42]. That is the case off the coasts of Iberia and north-west Africa (Canary Current), but also along the coasts of California–Oregon (California Current), of Peru–Chile (Humboldt Current), of Namibia–Angola (Benguela Current), and of West Australia (West Australian Current). The synoptic pattern responsible for these coastal winds (a high pressure over the ocean and a thermal low inland, resulting on a land-ward pressure gradient), that drive the wind driven Canary Current [43], starts to build during late spring and can last as far as early fall. Nevertheless, in some areas, due to the prevalence of the high-pressure cell over the ocean and to enough radiative heating inland, equator-ward along coast winds can also occur during winter [42]: along the Peru–Chile and Namibia–Angola coasts and, to a certain extent, also the north-west African coast [40].

In most areas of the world's oceans, more than 75% of the time, the wave field is dominated by swell (swell waves are more prevalent; [11]), with the exception of the intense wind speed belts in the mid to high latitudes. Nevertheless, some areas experience a strong seasonality of the wave-field

characteristics, mainly in marginal or enclosed seas [20,26,44,45]. This is also the case EBC systems [7]. Coastal winds along EBC systems are strongly linked to regional ocean dynamics, with impacts both in the atmosphere and the ocean through an intrinsic atmosphere-ocean coupling process [46]. The major upwelling zones occur along EBC systems. These areas are among the most productive fisheries of the global ocean, due to the cold nutrient-enriched upwelled bottom waters that give rise to very rich biological activity at the surface. Although, the interaction between these winds features and upwelling has been relatively well studied [45–50] that is not the case with the regional wave climate. Concerns about waves and sea-state forecast on the western coasts of Morocco go back to early twentieth century, when an early warning system to the incoming of winter swells that could seriously limit harbor operations in Casablanca was developed by the French Navy, in collaboration with the Portuguese Weather Office in the Azores [51]. More recently the Moroccan authorities have shown similar concerns related to beach erosion and how waves are affecting beach morphodynamics [52]. Nevertheless, no study has addressed the regional wave climate in that area, as well as on the west coast of Iberia, using a qualitative approach taking into account the seasonal variability of the winds. Integrated in global [39,40], and regional studies [53,54], looked at western Iberia and north-west Africa wind field characteristics, with a particular focus on coastal jets. They have concluded that the marine winds field along the Canary EBC system can be seen as unique, in the sense that the Canary current is disrupted by the influx of Mediterranean (denser) water, into the North Atlantic basin, but also by the Azores current closer to the surface. The coastline is also different from other CLLJ areas, since its continuity is disrupted by the Gulf of Cadiz. The prevalent boreal summer coast parallel atmospheric flow along the equator-ward Canary Current has, therefore, two separated centers of action: along the west coast of the Iberia and along the north-west African coast, from Morocco to Mauritania.

Here we present a detailed study of the wave climate along the eastern boundary Canary Current system (EBCCS). The study is based on the European Centre for Medium-Range Weather Forecasts (ECMWF) reanalysis ERA-Interim [55]. The regional distribution and seasonal variation of the wind sea and swell SWH and MWP parameters, and how they combine in the total SWH and MWP, are presented. The analysis of the prevalence of one type of waves over the other, from an energy and predominance point of view, is also shown.

The remainder of the paper is organized as follows. The ERA-Interim reanalysis, the buoy data, and the methodology of the study are described in Section 2. Details about how wind sea and swell parameters are computed are also presented in Section 2. The ERA-interim performance evaluation is shown in Section 3. Section 4 presents the climatology of the regional wind sea and swell characteristics. The paper ends with summary and concluding remarks, as well as with suggestions for further research in Section 5.

2. Data and Methods

2.1. ERA-Interim

ERA-Interim is a third generation global reanalysis of meteorological observations produced by ECMWF. The ongoing project was supposed to go back only to 1989, but in 2011 the reanalysis was extended further backwards to 1979. Here we use the period from January 1979 to December 2014. Besides atmospheric variables, the ERA-Interim also includes wave parameters, since it was produced using the Integrated Forecasting System (IFS; release cycle Cy31r2, used operationally at ECMWF during the period December 2006 through June 2007), a two-way coupled atmosphere-wave model system [56]. The wave model used in the coupled system is the third-generation WAVE Model WAM model [57]. The horizontal resolution of the atmospheric model is approximately 79 km (T255 spectral truncation) on a reduced Gaussian grid. The wave model is run with shallow-water physics, with a horizontal resolution of approximately 110 km. The temporal resolution of ERA-Interim is 6 h. Observations of ocean wind speeds from VOS (voluntary observing ships), buoys, and satellite

scatterometer, were assimilated in the reanalysis process. Since 1991 satellite altimeter wave heights were also assimilated. In situ SWH measurements and altimeter winds at 10 m heights are not used in the ERA-Interim so they can serve to independently evaluate the merits of the reanalysis. A 4DVAR (four-dimensional variational) data assimilation scheme was used in ERA-Interim. The WAM model set up in the ERA-Interim reanalysis uses the 2-min gridded elevations/bathymetry data for the world (ETOPO2). In spite of its relatively coarse resolution, since it is a global product, ERA-Interim is a dataset of superior quality, comparing very well with buoy observations. Additional details about the ERA-Interim reanalysis and its comparison with other global wave hindcasts can be found in [55,58] and [59], respectively.

2.2. Buoy Data

In situ wave observations from five directional Waverider buoys, moored off-shore the west coasts of Iberia (in the vicinity Vigo, in Spain, at $43^{\circ}28'48''$ N– $009^{\circ}13'12''$ W), and offshore Leixões, at $41^{\circ}19'$ N– $008^{\circ}59'$ W, and Sines, at $37^{\circ}55'16''$ N– $008^{\circ}55'44''$ W, in Portugal), south of Portugal (in the vicinity of Faro, at $36^{\circ}54'17''$ N– $007^{\circ}53'54''$ W), and in the Canary Islands (north-west of Gran Canaria, at $28^{\circ}10'48''$ N– $015^{\circ}49'12''$ W) are used here. The buoy positions can be seen in Figure 1. These buoys are owned and maintained by *Puertos del Estado* (Spanish Buoys) and by the Portuguese Navy Hydrographic Institute (Portuguese buoys). The data used here covers the period from 1991 to 2014. The in situ wave measurements are used for the evaluation of ERA-Interim, and were not used in the ERA-Interim data assimilation process.

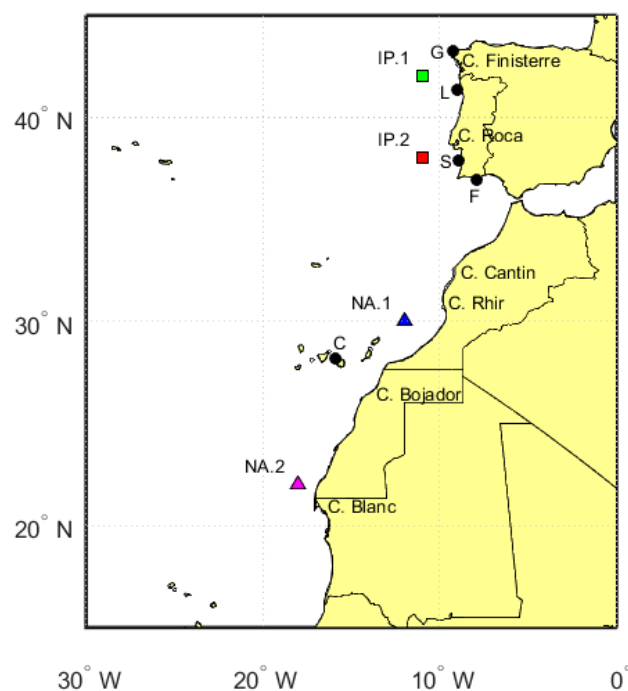


Figure 1. Map with buoy positions with black dots: G-Galicia Villano ($43^{\circ}28'48''$ N– $009^{\circ}13'12''$ W), L-Leixões ($41^{\circ}19'$ N– $008^{\circ}59'$ W), S-Sines ($37^{\circ}55'16''$ N– $008^{\circ}55'44''$ W), F-Faro ($36^{\circ}54'17''$ N– $007^{\circ}53'54''$ W), and C-Canary Gran Canaria ($28^{\circ}10'48''$ N– $015^{\circ}49'12''$ W), and key positions along the west coast of Iberia Peninsula (green and red triangles: IP.1, and IP.2, at 42° N– 11° W, and 38° N– 11° W, respectively) and the north-west coast of Africa (blue and magenta squares: NA.1, and NA.2, at 30° N– 12° W, and 22° N– 18° W, respectively).

2.3. Spectral Partition and Wave Parameters

The wave parameters used here are computed from the two-dimensional (2D) wave-energy spectra outputted at each grid point by the wave model WAM in the coupled IFS. From the

wave-energy spectra [$E(f, \theta)$, where f is the frequency and θ the propagating direction] several integrated parameters can be computed, including the wind sea and the swell wave parameters. In the present study the SWH, MWP and mean wave direction (MWD) parameters from the total (H_s, T_m, θ_m), swell (H_s^s, T_m^s, θ_m^s), and wind sea (H_s^w, T_m^w, θ_m^w) wave fields, respectively, and besides that the wind speed and wind direction at 10 m height (U_{10} and φ , respectively) are also used. The wind sea and the swell parameters are computed by integrating over the high- and low-frequency parts of the energy-wave spectra, respectively, which is separated by a characteristic frequency \hat{f} , corresponding to a wave phase speed:

$$\hat{c} = 1.2 \times 28 \times u_* \cos(\Delta) \quad (1)$$

where u_* is the friction velocity, and Δ is the difference between the wave propagating direction and the wind direction ($\Delta = \theta - \varphi$), and $\hat{c} = g(2\pi\hat{f})^{-1}$. The WAM partition scheme is rooted in the Pierson–Moskowitz spectrum [60,61], and based on the wave age parameter, being different from other partition schemes, like the one from [32] used in WW3 and CFSR [59]. The factor 28 corresponds to the peak wave phase speed from the Pierson-Moskowitz spectrum and 1.2 is a tuning parameter. Further details on the WAM wave model and on the spectral separation scheme can be found in [7,26,62].

2.4. Methodology

To assess the wind sea and swell wave climates along the EBCCS, the ERA-Interim wind and wave parameters were processed seasonally, following the WMO (World Meteorological Society) standards, seasons are named (for the northern hemisphere) as: DJF (December to February; Winter), MAM (March to May; Spring), JJA (June to August; Summer), and SON (September to November; Fall). The climatological analysis is based on the DJF and JJA seasons, in spite of some remarks in the text concerning MAM and SON. We look preferably to the boreal summer and winter seasons since they can be viewed as “extreme” seasons regarding the wind and wave climates in the North Atlantic sub-basin [63]. Following the same reasoning, MAM and SON will be considered here as “intermediate” seasons.

The quality of the ERA-Interim output in the area is assessed by comparison with wave height (H_s) observations from five buoys (see Figure 1). Wave heights from the nearest ERA-Interim grid point were interpolated to the buoy positions through bilinear interpolation. The linear trend, BIAS, root mean square error (RMSE), and correlation coefficient (r) of the ERA-Interim to the in situ observations, are also computed.

The mean wind sea (H_s^w, T_m^w) and swell (H_s^s, T_m^s) parameters are compared for the DJF and JJA seasons. Extreme wind sea and swell wave heights (percentile 99%), are also compared for those seasons, as are the relative seasonal wind sea and swell energy fluxes E_f^w and E_f^s , respectively, as well as the respective spectral energy contents E^w and E^s , respectively. The intra-annual variability of the total (H_s, T_m), wind sea (H_s^w, T_m^w) and swell (H_s^s, T_m^s) parameters, in the context of the yearly variation of the local wind speed (U_{10}), is shown.

3. ERA-Interim Evaluation

The results of the evaluation of the ERA-Interim, along the EBCCS and south of Portugal, are shown in the Figure 2 scatter plot. Daily measured and modeled mean values of H_s are compared. The ERA-Interim H_s compares very well with the in situ measurements, slightly under-forecasting wave heights, with a total (from the five buoys) BIAS and RMSE of -0.19 m and -0.18 m, respectively. The total correlation coefficient can also be considered high ($r = 0.94$). For this reason, despite its relative coarse resolution, ERA-Interim proves to be a very good wave product, which can be used to reproduce and analyze the wave climate in the area of study.

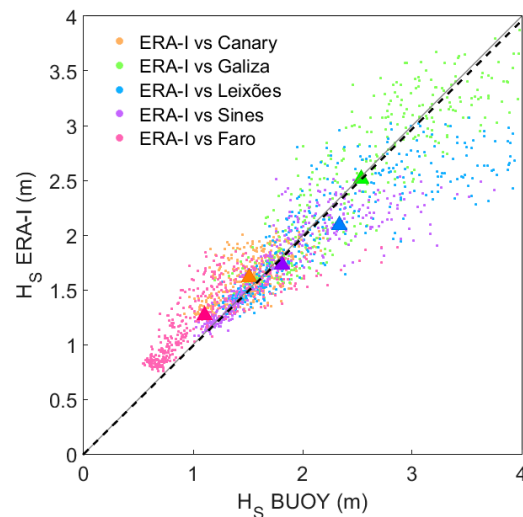


Figure 2. Scatterplot of daily mean in situ measured versus ERA-Interim H_s from the five buoys in Figure 1. Each dot in the background corresponds to a daily mean comparison. The linear fit (black dashed line) has been computed for the total dispersion from the five buoys. The triangles correspond to the full means.

4. Results

4.1. Wind Sea and Swell Wave Heights and Periods

The wind speed in the North Atlantic sub-basin, in DJF, is highest along the extratropical storm tracks. In JJA, when the Westerlies are weaker, due to a lower extratropical cyclonic activity, the wind speed in the North Atlantic tends to be highest along the EBCCS (and in the Caribbean Sea; [7,39,40]). The DJF and JJA seasonal means of U_{10} and φ in the EBCCS area are shown in Figure 3. In DJF (Figure 3a) the climatological mean winds are from the west along the west coast of Iberia, veering in the Gulf of Cadiz to become north and north-east (coast parallel) along the coasts of Morocco and Western Sahara. During JJA (Figure 3b), due to the presence of the Azores High around 35° N, the wind is almost always coast parallel, from Iberia to Mauritania, with notorious seasonal differences between DJF and JJA. The winter mean wind speed along the EBCCS, particularly close to the coast, is $\sim 6.5\text{--}7\text{ m}\cdot\text{s}^{-1}$ from Iberia to Cap Blanc (henceforth called Cape Blanc), increasing to $\sim 7.5\text{--}8\text{ m}\cdot\text{s}^{-1}$ south-ward from there. During summer the wind-speed pattern in the area is substantially different, with the highest wind speeds occurring closer to the coast, particularly along Morocco until Cape Blanc, with two distinct high wind-speed areas (close to $9\text{ m}\cdot\text{s}^{-1}$) north and south of Canary Islands. These mesoscale intensifications of the surface wind speed along the coast in the EBCCS area, on the north-west African coast, occur due to the sharpening of the pressure gradient there through a positive feedback process triggered by upwelling and by the low SST at the coast [64–67]. The low SST decreases the air temperature within the MABL at the coast, and a sharp inversion develops due to warm subsiding air above [68,69]. The decreasing MABL air temperature towards the coast causes the capping inversion to slope gently from west to east, leading to the channeling of the flow at the coast that, due to a Bernoulli effect, leads to a wind-speed increase [46]. This feature is sometimes accompanied with the occurrence of coastal jets in summer, with the wind speed increasing in altitude, with maxima around the MABL height, at altitudes of the order of 400–600 m [39,40,53,54,70–72]. The presence of headlands as well as the orientation of the coast line can also result in additional local enhancement of the wind speed at the coast [41,68,73], as well as in changes in the flow direction. When the flow interacts with points and capes protruding off the coast, gravity waves are excited. These gravity waves propagate on the MABL inversion and are responsible for the adjustment of the flow that leads to changes in the wind speed and direction in the lee of the headlands. The wind-speed maxima north and south of the Canary Islands are the cumulative result of flow channelling and flow

interaction with coastal topography, namely with Capes Cantin and Rhir (Morocco), Cape Bojador (Western Sahara) and Cape Blanc (Mauritania)—the positions of these capes can be seen in Figure 1. Clearly the wind direction backing south of Cape Blanc is an expansion fan effect [41,73].

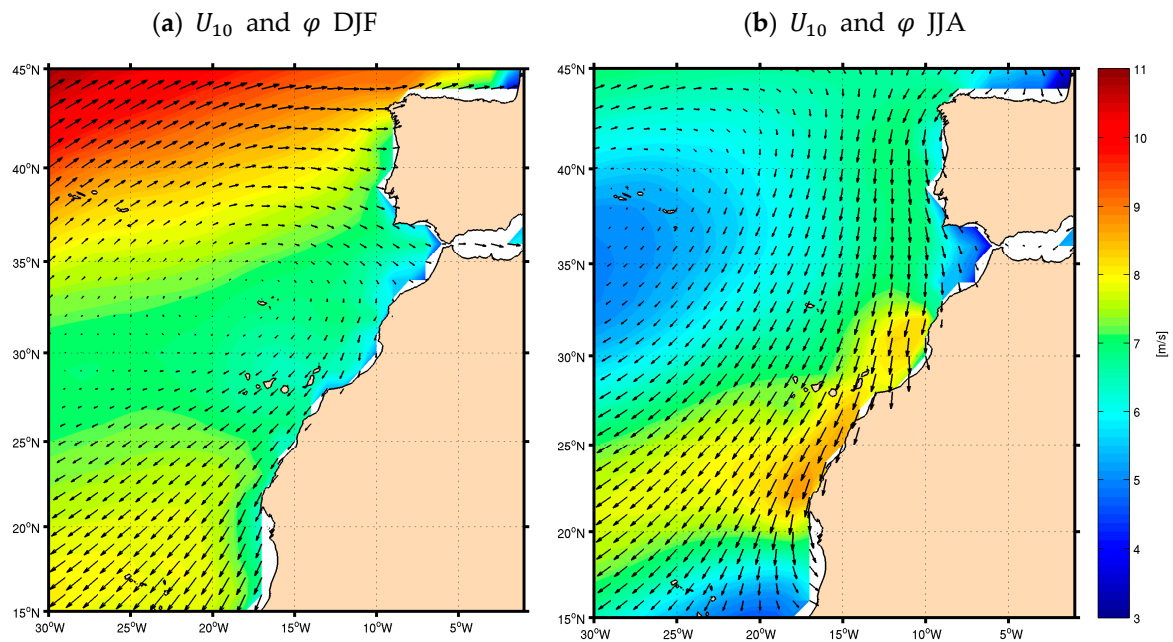


Figure 3. Climatological averages of U_{10} ($\text{m}\cdot\text{s}^{-1}$) and φ ($^{\circ}$) for (a) December to February, Winter (DJF) and (b) June to August, Summer (JJA). The arrows are scaled with the corresponding background fields.

The seasonality of the DJF and JJA wind-field characteristics along the EBCCS, drive the wave-field seasonal differences in the area, with noticeable consequences on the wave heights and in the overall wave-field characteristics. The winter and summer maps of the climatological mean H_s , H_s^s , and H_s^w are shown in Figure 4. The mean H_s fields in the area of study are substantially different from winter to summer. The reason for these differences, lie in the synoptic and regional seasonal wind-field patterns, and can be explained with the H_s^s , and H_s^w fields and in the way they combine in the total H_s . In DJF, when winds are weaker along the EBCCS and stronger along the extratropical storm tracks, from $\sim 40^{\circ}$ N to $\sim 65^{\circ}$ N (not shown here, but present in the north-west area of the map in Figure 4a), the wave field is mostly the result of swell waves propagating into the area from the central North Atlantic [7]. The climatological mean DJF H_s^s (Figure 4c) along Iberia is about 2.5–3 m, while the H_s^w mean (Figure 4e) there is clearly less than 1 m. Along the coasts of Morocco to Mauritania the difference is even higher, since the mean H_s^w , due to the low winter wind speed there, is only about 0.5–0.7 m, or even lower than that in some areas. Note the sheltering effect of the Canary Islands, leading to lower wave heights mostly along the coasts of Western Sahara. In JJA higher wind speed along the EBCCS is responsible for the local generation of waves, and hence for higher climatological mean H_s^w (Figure 4d), compared to winter. Along the Iberian west coast the summer H_s^s (1.5–1.7 m; Figure 4f) is still higher than H_s^w (about 1.3–1.4 m), but along the coasts of Morocco and Western Sahara, particularly in the latter until Cape Blanc, the mean H_s^w is higher than H_s^s . In DJF the climatological mean wave heights along the EBCCS are clearly dominated by swell (i.e., $H_s^s > H_s^w$; Figure 4c,e), reflecting the remotely generated waves and the strength of the westerly winds along the extratropical storms tracks at higher latitudes. In JJA, swell waves are still higher along west Iberia (although the H_s^s and H_s^w mean fields are more comparable there than in the winter). That is not the case along the coast of north-west Africa, from Morocco to Mauritania, where now $H_s^s < H_s^w$ in some areas (Figure 4d,f), due to the high summer wind speeds there (Figure 3b), but also, to a certain extent, to the sheltering effect of the Canary Islands.

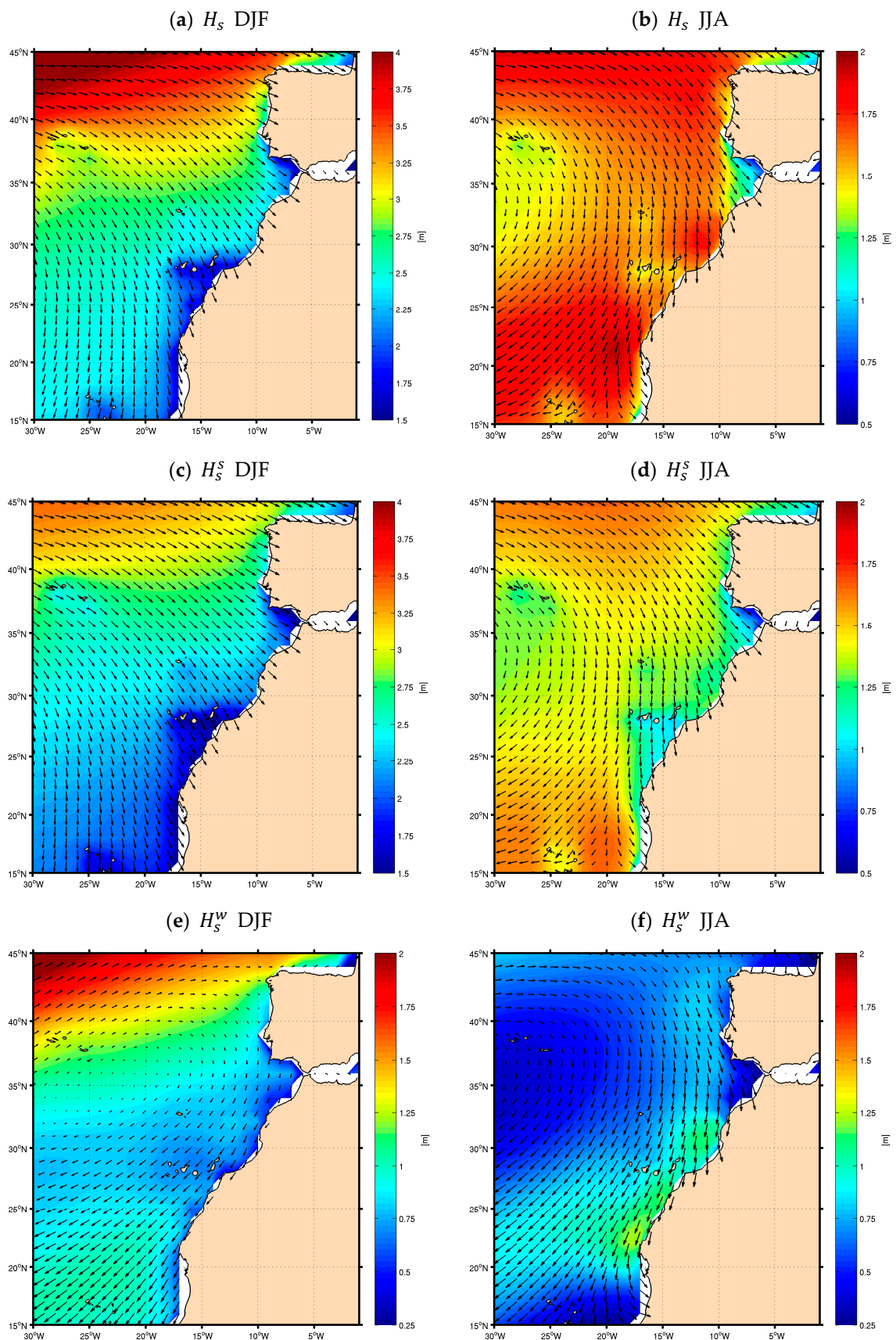


Figure 4. Climatological averages of H_s (m) for (a) DJF and (b) JJA, of H_s^s (m) for (c) DJF and (d) JJA, and of H_s^w (m) for (e) DJF and (f) JJA, as well as of θ_s ($^\circ$), θ_s^s ($^\circ$), and θ_s^w ($^\circ$) for the corresponding seasons. The arrows are scaled with the corresponding background fields, and the color scales vary between the different panels.

When the wind sea and swell extreme wave heights along the EBCCS are evaluated, the differences between the DJF and JJA H_s^s and H_s^w fields are considerably larger. In Figure 5 the winter and summer maps of the climatological 99% percentiles are shown. The annual and seasonal percentiles were computed for every year and then averaged. It can be seen that the extreme wave heights along the EBCCS are dominated by swell in DJF (Figure 5c,d), even in the sheltered area east of the Canary Islands (with $H_s^s > H_s^w$), as a result of waves that have propagated from the extratropical storms at higher latitudes in the central North Atlantic. Nevertheless, 1% of the time during winter H_s^w along Iberia can still reach values of the order of 4–4.5 m or more (Figure 5e). These DJF locally generated waves are generated by winter land falling frontal systems in the west coast of Iberia (not shown), when the North Atlantic Oscillation (NAO) is at its negative phase [74–76]. The frontal storms are responsible for very high wind speed events, usually from the south-west, before the cold front passage, veering to the north-west sector after the front. In JJA the situation is different [77]. The extreme wave heights in the area are now clearly dominated by wind sea ($H_s^s < H_s^w$), from west Iberia to Mauritania, with the exception of an area west of the Gulf of Cadiz, North of the Madeira Islands, reflecting the particular characteristics of the wind and wave climates along the EBCCS due to the influx of Mediterranean water and to the Azores Current [78]. During summer, along the EBCCS, extreme wave events are locally generated, particularly in the northern part of the west coast of Iberia, where 1% of the summer H_s^w can be as high as 3 m or more. The highest 99% percentile H_s^w values occur in the lee of coastal headlands: Cape Finisterre, Cape Cantin, and Cape Blanc, where the wind speed increases due to the interaction of the flow with the coastal headlands [39,41,53,71]. The MWD of the wind sea and swell extreme waves along the EBCCS (not shown) is consistently similar to the mean ones shown in Figure 4.

As waves grow and propagate away as swell from their generation area, they become shallower (the wave height decreases) and longer (in wave length and period). Long waves reaching a shore are a sign of remotely generated waves (old swells), whereas shorter waves reaching the same shore, are waves that were generated closer (young swells). On the other hand, under the influence of high wind speeds the ocean surface will, until it gets saturated, have “longer” wind seas since their phase velocity is still lower than the wind speed. As shown above (Figure 3) the area of study is clearly under the influence of two different wind regimes, in winter and summer. For that reason, the local mean wave periods should also reflect the seasonal differences of the local wind field. Figure 6 depicts the DJF and JJA maps of the mean T_m , T_m^s , and T_m^w along the EBCCS, where these seasonal differences can be seen. The seasonal differences between winter and summer total, swell, and wind sea mean periods regimes can be considered even more striking than the wave heights. During DJF the mean periods are longer along Iberia (Figure 6a), increasing from the central North Atlantic sub-basin towards south-west Europe and Morocco, with values of the order of 10–10.5 s. A clear wave front propagates from the North Atlantic mean winter storm path towards Iberia and Morocco. Again, the sheltering effect of the Canary (and Madeira) Islands has an effect on the winter T_m field, which starts to decrease southward closer to Cape Blanc due to the effect of the winter North Atlantic trade winds, from the coasts of western Sahara towards the west. These long-period winter waves reflect the propagation of waves generated farther north, which is clearer in the DJF mean T_m^s field (Figure 6c). The winter wind sea mean periods (Figure 6e) reflect the high wind speeds at higher latitudes, and the effect of the North Atlantic trades in the south part of the area of study. The DJF mean T_m^w are low along the coast from Iberia to Mauritania. During JJA the effect of the local winds in the mean wave periods along the EBCCS is much higher than in winter. From Cape Roca until Cape Blanc the mean JJA T_m (Figure 6b) is the lowest in the area (6.5 to 7 s), corresponding to higher mean T_m^w (Figure 6f) due to the high wind speeds in that area. The JJA swell mean periods (Figure 6d) reflect an influx of southern hemisphere waves, with the highest mean T_m^s (higher than 9 s) south of the Canary Islands. Cross swells can be expected in that area. The Cape Verde islands’ sheltering effect should be noted. Wind sea mean periods during JJA are lower in the areas where the wind speed is highest, reflecting the expansion fan effect, on the wave field leeward of coastal headlands, from Cape Cantin to Cape Blanc.

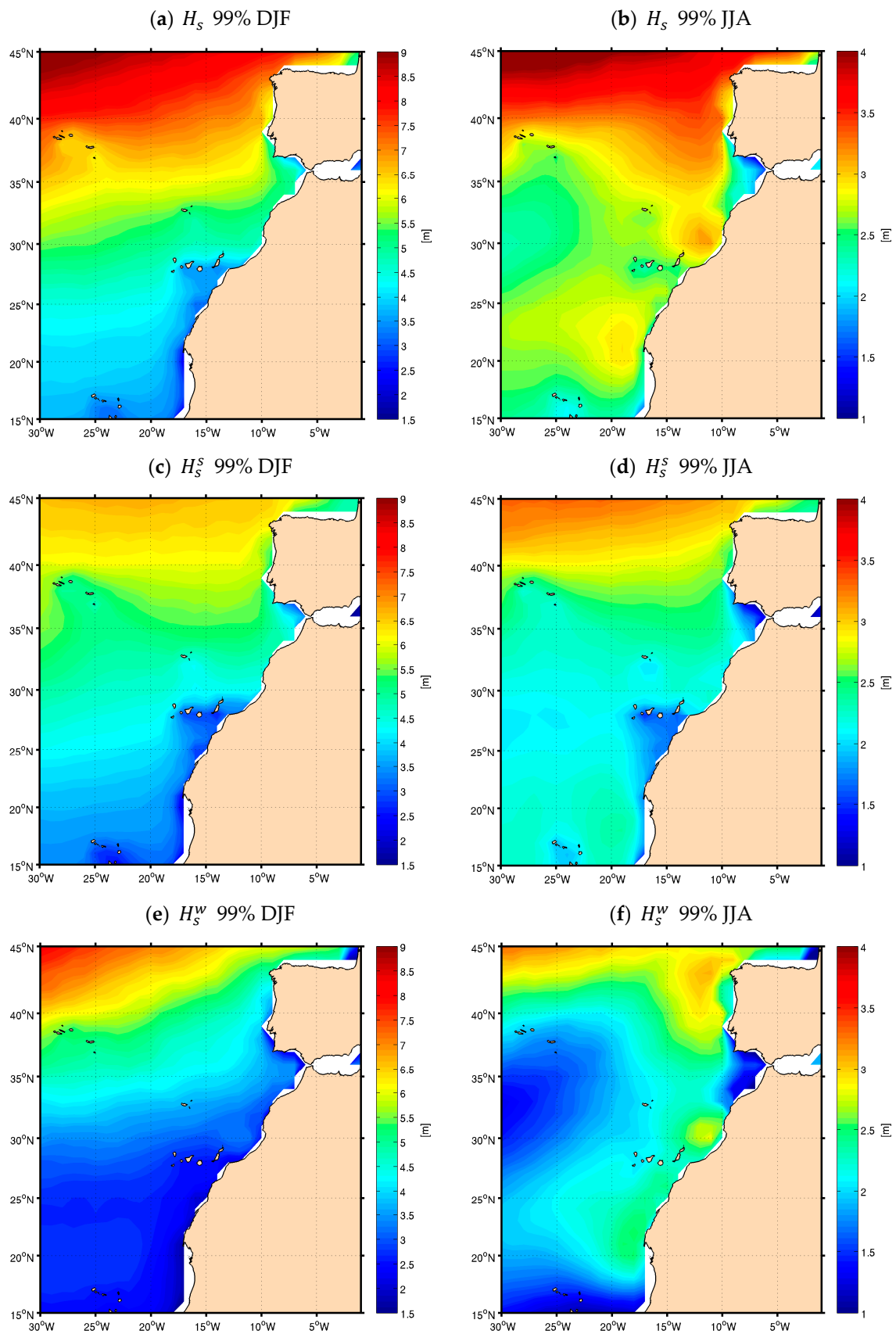


Figure 5. Climatological averages of the 99% percentiles of H_s (m) for (a) DJF and (b) JJA, of H_s^s (m) for (c) DJF and (d) JJA, and of H_s^w (m) for (e) DJF and (f) JJA. The color scales vary between seasons.

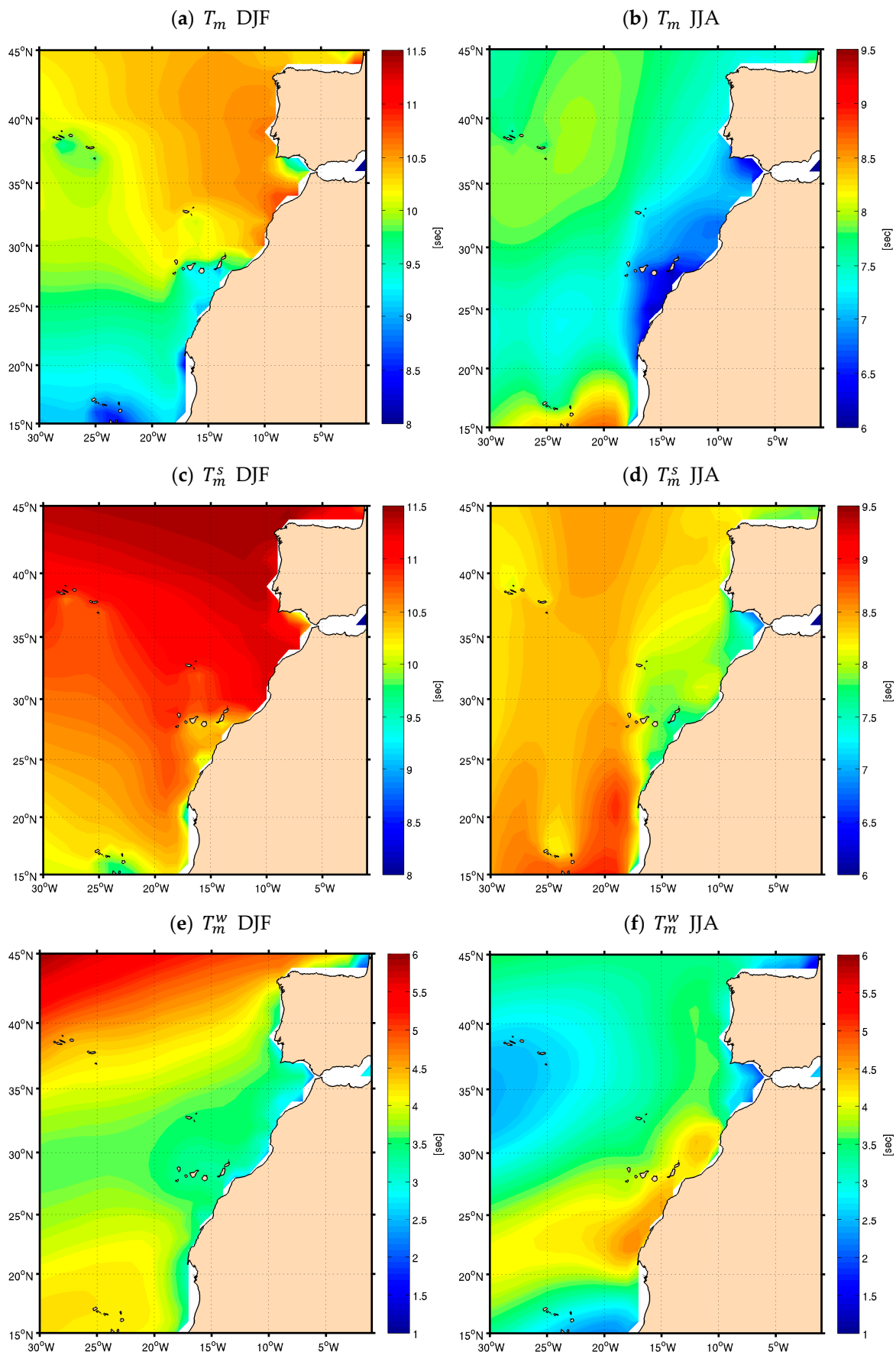


Figure 6. Climatological averages of T_m (m) for (a) DJF and (b) JJA, of T_m^s (m) for (c) DJF and (d) JJA, and of T_m^w (m) for (e) DJF and (f) JJA. The color scales vary between panels.

The DJF and JJA ratio of H_s^s , and H_s^w is shown in Figure 7. In these maps, the relative weight between swell and wind sea wave heights is depicted, allowing a more quantitative assessment between the heights of the two types of waves. Values higher (lower) than 1, mean that swell (wind sea) waves are higher, and values closer to 1 mean that H_s^s and H_s^w are comparable. During winter, swell wave heights are always higher than wind seas throughout the area of study, as shown in Figure 4. In winter (Figure 7a), the differences between H_s^s and H_s^w are highest in a band extending south-west from Iberia and the Atlantic coasts of Morocco (where swell height are 3 to 3.5 times higher than wind seas). The differences between H_s^s and H_s^w are lower north of Azores and south of Canary Islands, due to the high wind speeds along the extratropical storms tracks and along the North Atlantic trades, that generate higher wind sea waves. Swell heights there are on average around 2 to 2.5 times higher than wind seas. The sheltering effect of the Canary Islands, lowering the swell wave heights southward from there, is not negligible. In JJA the differences between H_s^s and H_s^w (Figure 7b) are highest in the Azores (3.5 to 4 times higher than wind seas), and offshore Senegal around 15° N–17° N (more than 5.5 times higher, due to southern hemisphere swells). The differences between the two types of waves is lower along the Canary Current path, however, from west Iberia until the North Atlantic trades south-west of Canary Islands (with swell waves being on average about 1.5 to 1.7, or less, higher than wind seas). The high wind speeds in summer, along the north-west coast of Africa, from Cape Cantin to Cape Blanc, are responsible for the highest H_s^w values there. In JJA, in that area, swell wave heights are on average lower (about 10% to 20%) than wind seas. The similarity between the DJF and JJA H_s^s and H_s^w ratio and the T_m^w shown in Figure 6e,f should be noted, reflecting the locally generated waves effect.

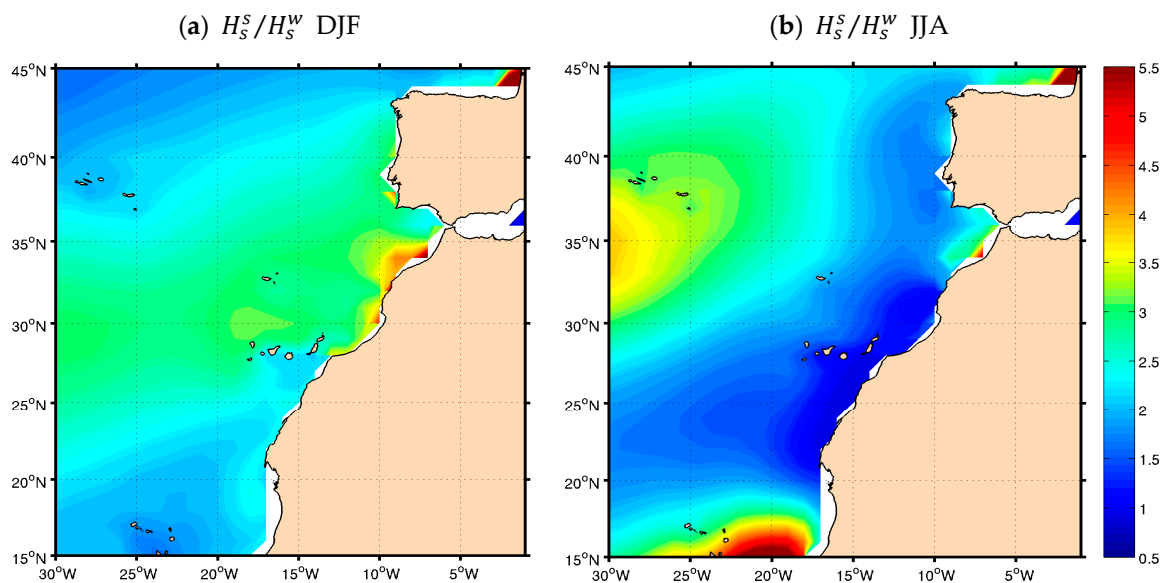


Figure 7. Climatological distribution of the H_s^s / H_s^w index (dimensionless), for (a) DJF and (b) JJA.

4.2. Wind Sea and Swell Wave Energy

Assessments of global wave-energy flux (or wave power per unit crest, $\text{KW}\cdot\text{m}^{-1}$) have been receiving increasing attention in the scientific literature [79,80]. Nevertheless, regional studies of the wave-energy flux are still lacking, despite the fact that the wave power is the quantitative representation of the ability of waves to perform work, on a shore or on off-shore infrastructures, for example, and is the most important parameter for wave-energy harvesting. A qualitative analysis of the wave power is very important, since that should reflect the locally generated wave power and the wave power that is transferred from one area of the ocean to another. The wave energy flux is defined as:

$$E_f = AT_m(H_s)^2 \quad (2)$$

where $A = \rho g^2 / 64\pi$ is a constant (ρ is the water density and g the gravitational acceleration). The swell and wind sea wave-energy fluxes are, in turn, defined as $E_f^s = AT_m^s (H_s^s)^2$ and $E_f^w = AT_m^w (H_s^w)^2$, respectively. The winter and summer climatological means of E_f , E_f^s , and E_f^w are depicted in Figure 8. During winter, in the area of study, waves carry considerably more energy than in summer (3 to 4 times more; Figure 8a), and this energy is mostly concentrated in the swell (low-frequency) part of the wave spectra (Figure 8c). In DJF, swell waves reaching the coasts of Iberia and north-west Africa are still relatively high (Figure 4c) and long (Figure 6c). On the other hand, wind sea waves, due to the relatively lower wind speeds (compared to JJA; Figure 3), are low in height and carry less energy. In summer, the wave-power pattern changes. There is an influx of southern hemisphere swells (not very high but very long; Figures 4d and 6d) that contribute to the higher levels of wave energy offshore Mauritania (Figure 8b). Although considerably less frequent and energized in JJA [2,7,59], extratropical storms are still the major source of wave energy carried by swell waves in the area. Wind sea wave power in summer is only present in the high wind-speed areas, in the northern part of the west Iberian coasts, and along the coasts of Morocco and Western Sahara. In these areas, however, E_f^w is comparable (in Iberia) or even higher (in Africa) to E_f^s .

Besides the ratio between swell and wind sea wave heights (Figure 7), it is also important to understand comparatively which type of waves carry more energy in the area of study. The swell and wind sea energy densities per unit area (in $J \cdot m^{-2}$) were computed for swell ($E^s = \rho g m_0^s$) and wind sea ($E^w = \rho g m_0^w$), m_0^s and m_0^w are the swell and wind sea *zeroth* spectral moments, respectively, and

$$m_0 = \iint f^0 E(f, \theta) df d\theta \tag{3}$$

is the generic spectral zeroth moment. The maps of the DJF and JJA swell spectral-energy proportions (or spectral weight, w_s) to the total energy carried by the waves (E^s / E ; where E is the total spectral wave energy density, define as $E = \rho g m_0$) are shown in Figure 9. The wind sea energy weight (not shown) is $E^w / E = 1 - E^s / E$. During winter, swells clearly carry most of the energy throughout the entire area of study (Figure 9a), with the highest percentage (85–90%) along the coasts of Iberia and Morocco. Swell energy weight is slightly lower in the northern (southern) part of the area of study (75–80%), due to the winds generated under the extratropical storms (North Atlantic trades), as mentioned above. In summer (Figure 9b), when the wind speed increases considerably along the coasts of Iberia and north-west Africa, this relation is altered. The swell energy weight decreases along the Canary Current path (to 70–75% of the total energy), but increases (to 90–95%) at the Azores High area and more south due to the intrusion of southern hemisphere swells. On the other hand, from Cape Cantin to Cape Blanc, swell waves carry considerably less energy there: less than 60%, and even less than 50% in some areas, where the wave energy at the ocean surface is carried by locally generated waves. The summer local enhancement of wind speed in leeward of the most prominent capes along the north-west coast of Africa is clearly seen.

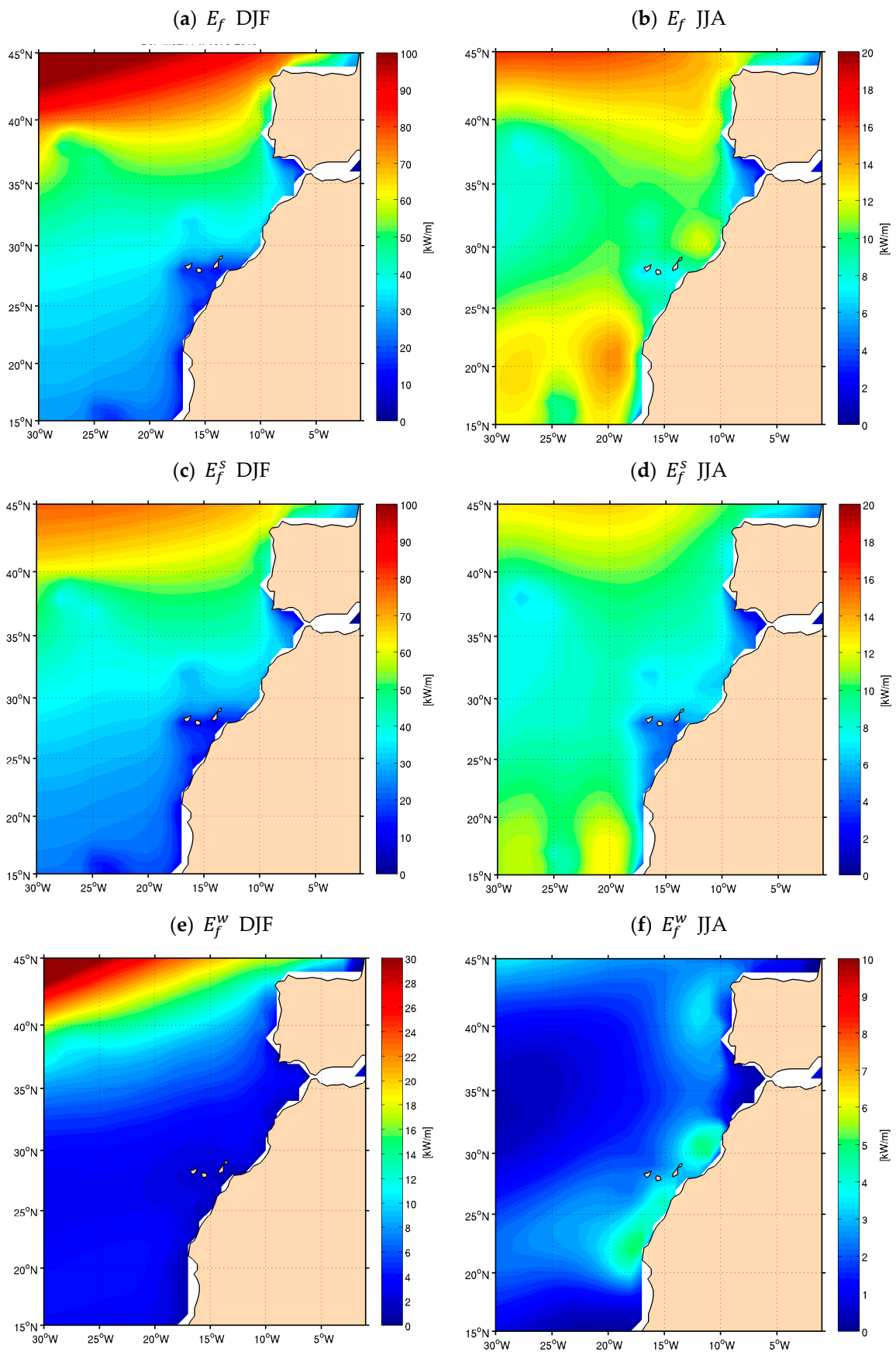


Figure 8. Climatological averages of the 99% percentiles of E_f ($\text{W}\cdot\text{m}^{-1}$) for (a) DJF and (b) JJA, of E_f^S ($\text{W}\cdot\text{m}^{-1}$) for (c) DJF and (d) JJA, and of E_f^W ($\text{W}\cdot\text{m}^{-1}$) for (e) DJF and (f) JJA. The color scales vary between seasons.

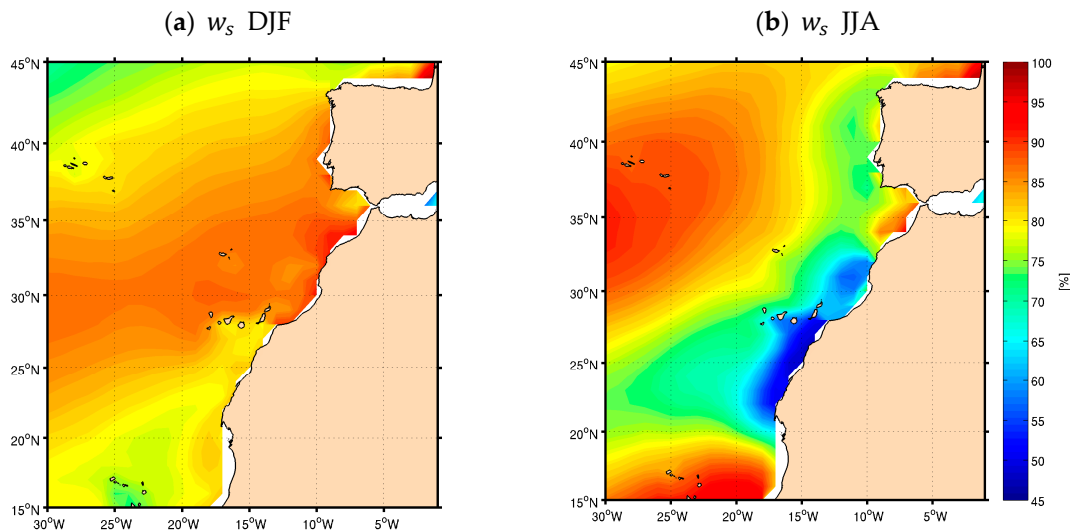


Figure 9. Climatological distribution of the swell spectral weight (w_s ; dimensionless) for (a) DJF and (b) JJA.

4.3. Wave-Field Characteristics

An alternative way to qualitatively assess sea state, or the type of waves at the ocean surface, is through the so-called wave age [17,56]. The wave age concept is based on the sheltering hypothesis of [81,82], and is defined as the relation between the peak wave phase speed and the wind speed at 10 m height (c_p/U_{10}), where $c_p = g(2\pi f_p)^{-1}$ is the peak wave phase speed and f_p is the peak frequency, i.e., the frequency of the wave component carrying more energy. Throughout the wave-age parameter, the developing stage of the waves can be assessed. From the Pierson and Moskowitz spectral theory [60,61,83] the sea state is considered under development (and dominated by wind sea waves) if $c_p/U_{10} < 1.2$, or mature (and dominated by swell waves) if $c_p/U_{10} > 1.2$. Figure 10 presents the probability of having swell-dominated wave fields along the EBCCS, in DJF and JJA, i.e., it presents the winter and summer probability of having a wave age higher than the fully developed threshold ($P_s = P(c_p/U_{10} > 1.2)$). The probability of having a swell dominated wave field was computed for DJF and JJA, following the approach of references [7,9,26]. At each grid point $P_s = N_s/N$, where N_s is the number of times $c_p/U_{10} > 1.2$ and N is the total number of events, was computed.

The DJF and JJA P_s maps are shown in Figure 10. In winter (Figure 10a) swell predominance is the rule throughout the entire area of study, with P_s around 90%, being higher (95% or more) in the winter swell band, from west Iberia to Morocco, towards the south-west. During summer (Figure 10b) the pattern changes due to the increased mean wind speed, but also to the decrease of the extratropical storms activity. The local increase of wind speed increases the presence of wind sea waves, hence lowering the probability of having swell-dominated wave fields along the coast. The Gulf of Cadiz is an exception to the decrease of swell prevalence in JJA along the EBCCS. From Cape Catin to Cape Blanc the values of P_s are much lower, reaching 50% or more, south of Cape Bojador. This means that in this area, during summer, the probability of having wind sea-dominated wave fields ($P_{ws} = 1 - P_s$) is substantial, i.e., on average locally generated waves prevail. The interesting aspect of the qualitative analysis of the wave field in the EBCCS, from the wave type prevalence is the substantial differences between ocean and coastal areas from Iberia to north-west Africa. Outside the Canary Current path, to the west in the open ocean, in JJA swell is clearly highly prevalent (with probabilities of occurrence close to 100% in the Azores area and south of 18° N).

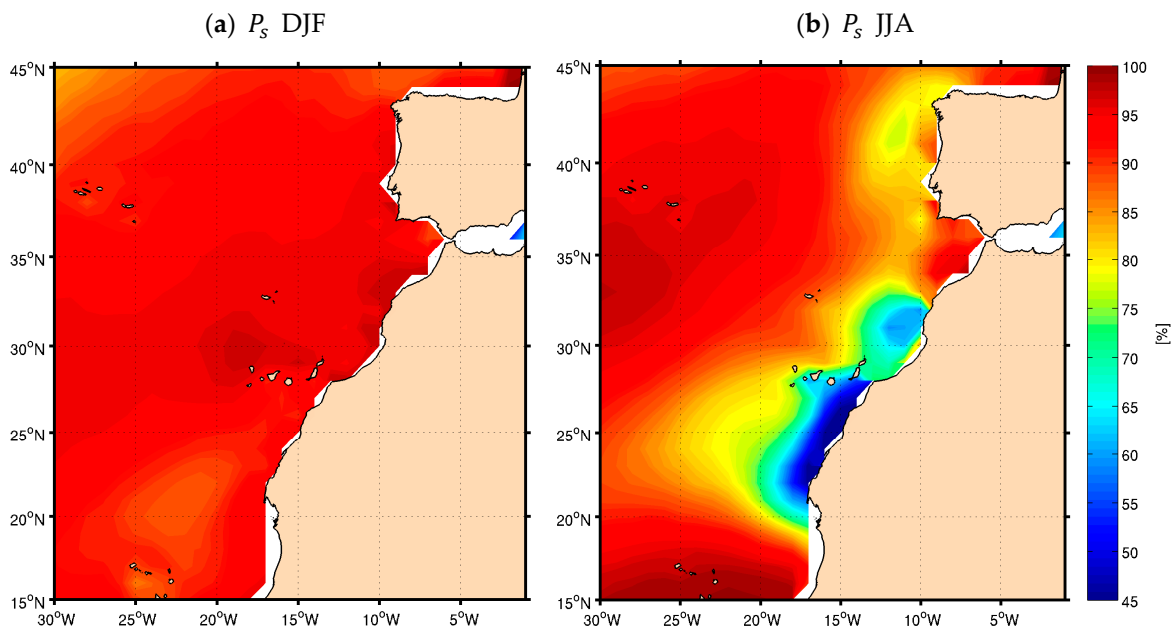


Figure 10. Climatological distribution of the swell prevalence (P_s ; dimensionless) for (a) DJF and (b) JJA.

Four key points (coinciding with ERA-Interim grid points) along the EBCCS were chosen to further investigate the wind sea and swell relation in the area of study: offshore west Iberia, IP.01 (42° N–11° W) and IP.02 (38° N–11° W), and the offshore north-west African coast, NA.01 (30° N–12° W) and NA.02 (22° N–18° W), as shown in Figure 1. The DJF and JJA $U_{10} - H_s$ scatter plots for these positions are shown in Figure 11 (Iberia) and Figure 12 (north-west Africa). In these scatter plots is overlaid the empirical relation between the SWH and the wind speed (line in red), presented by [60], as corrected by [61] for U_{10} , where:

$$H_s = 0.025U_{10}^2 \tag{4}$$

This curve corresponds to fully developed sea states (roughly where $c_p/U_{10} = 1.2$), and is seen as a separation between wind sea and swell. Values below (above) the line represent wind sea (swell) dominated sea states, i.e., with wave ages lower (higher) than 1.2. The color density in the scatter plots represents the data density normalized by the maximum values, in a non-dimensional scale.

During winter, in all four key positions (Figure 11a,c and Figure 12a,c) the scattering of the $U_{10} - H_s$ is high, indicating on the one hand a departure from the fully developed sea state (a characteristic of open oceanic waters), and on the other hand a high variability of the sea state (large number of wind speed vs. wave heights combinations). The high scattering is a characteristic on winter frontal weather across the North Atlantic sub-basin as mentioned by [2,7] where extratropical storms with different tracks (explained by the NAO phases), generating high waves, alternates with calm winds and long swells. High H_s values with low wind speeds represent swells traveling from northerly generated storms. This situation, in winter, is clearer at IP.01, IP.02 and NA.01 positions. The few situations with developing seas in DJF, in these three positions (more frequent at IP.01 and IP.02) are related to negative NAO phases, where storms track more south, with strong wind speeds related to land falling fronts at the peninsula. Swell domination is present in all four winter scatter plots, although less at NA.2 (Figure 12c), where the effect of extratropical storms and of incoming swell can be lower. At the three points north of NA.02, a large majority of U_{10} and H_s combinations on the “swell side” occur. In summer, the scattering is lower (as are wave heights), decreasing from IP.01 and IP.02 (Figure 11b,d) to NA.01 and NA.02 (Figure 12b,d). The lower scattering, and the higher concentration around the fully developed sea state curve (particularly at NA.01), is related to the lower

variability of the wind features [84], and consequently of the wave field, in JJA along the west coast of Iberia and the north-west coast of Africa. Besides the lower scattering (variability), a higher occurrence of wind sea-dominated situations (points under the fully developed sea state curve) occur at the four key positions (more at NA.01 and NA.02), compared to DJF. This situation is related to the summer local wind speed and wind sea features along the north-west coast of Africa.

4.4. Intra-Annual Variability

The intra-annual variability of the wind speed (U_{10}), MWP (T_m , T_m^s , and T_m^w), and SWH (H_s , H_s^s , and H_s^w) at the key positions IP.01, IP.02, NA.01, and NA.02 are show in Figure 13. The reader is advised that the graph panels in this figure have 3 scales: surface wind speed (top right), mean periods (middle left) and significant wave heights (bottom right). The intra-annual variability of the in situ (Figure 1) measured SWH from buoys G and L (Figure 13a), and S (Figure 13b), closer to the west coast of Iberia, and C (Figure 13c), in the Canary Islands, are also shown. The in situ SWH measurements are shown here not for the evaluation of ERA-Interim (since that has been done above; see Figure 2), but to show how wave height varies closer to the coast (west of Iberia) and within islands, where some sheltering takes place, west of north-west Africa.

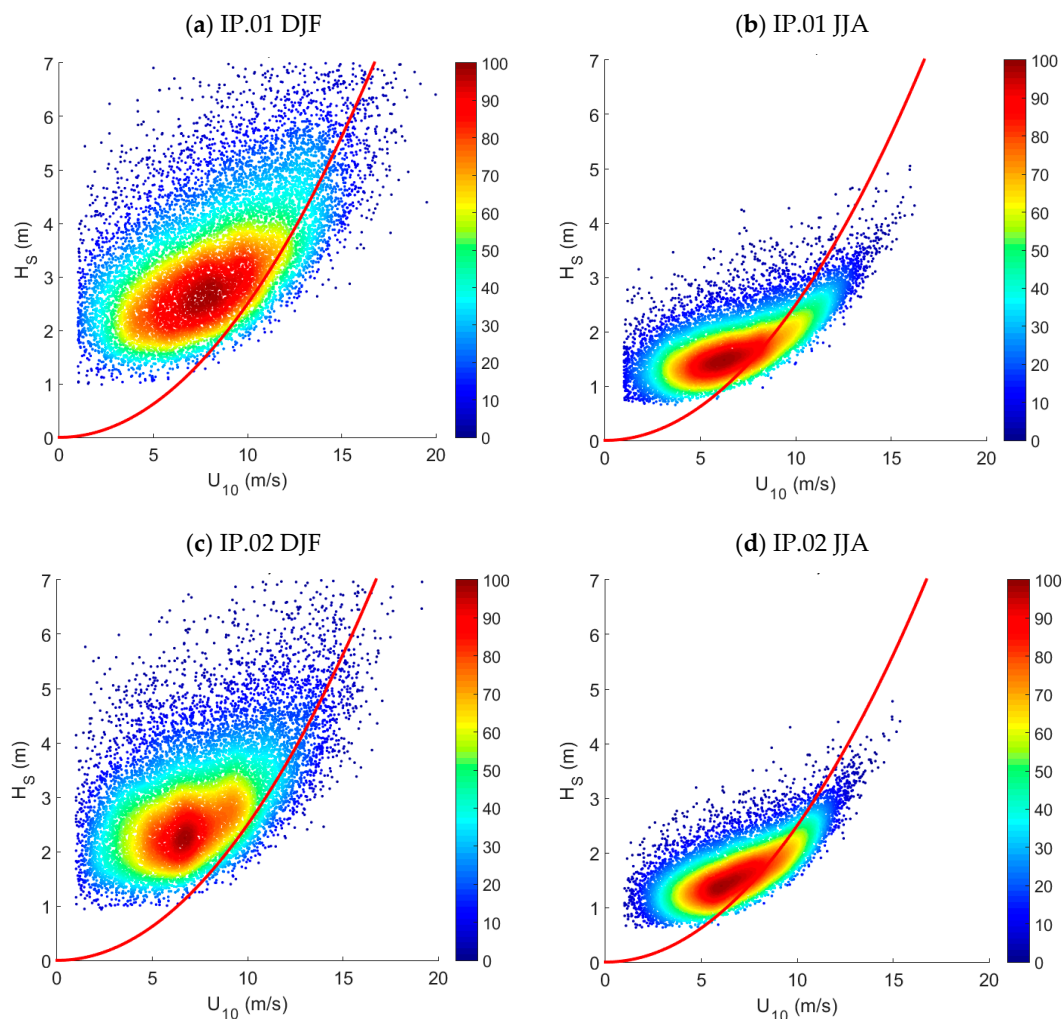


Figure 11. Scatter diagrams of U_{10} (ms^{-1}) and H_s (m) for position and IP.01 (at 42°N – 11°W) for (a) DJF and (b) JJA, and for key position IP.02 (at 38°N – 11°W) for (c) DJF and (d) JJA. The color density in the scatter plots represents the data density normalized by the maximum values, and the overlaid red lines represent the Pierson Moskowitz theoretical relation between U_{10} and H_s , a defined in Equation (4), for fully developed seas.

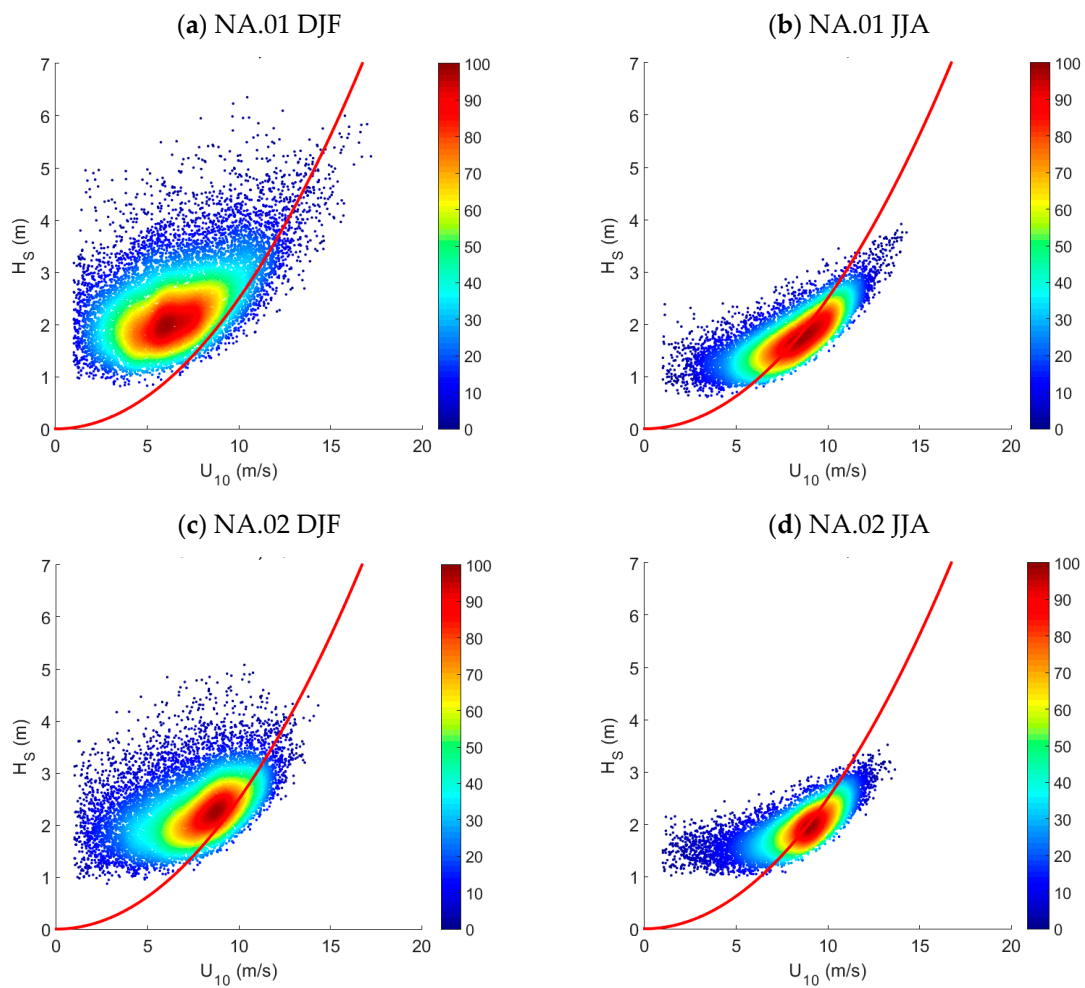


Figure 12. Same as Figure 10 but for key position and NA.01 (at 30° N–12° W) for (a) DJF and (b) JJA, and for position NA.02 (at 22° N–18° W) for (c) DJF and (d) JJA.

The U_{10} intra-annual variability at the three southernmost points show a gradual increase of the summer (June, July and August) mean wind speeds, particularly at NA.01 and NA.02, offshore north-west Africa, where the summer wind speed increase is notorious. That is not the case at IP.01, where U_{10} shows almost no variation during the year, nevertheless with a slight decrease during summer.

The summer wind speed increase is a particularly notorious increase at NA.01 (Figure 13c). At NA.02 (Figure 13d) the wind speed reaches its maxima in June, and from there on it gradually decreases, starting to increase again in January. The wind speed intra-annual variability at these points has an almost perfect correlation with the H_s^w intra-annual variability at the four positions (always higher than 0.97). A similar correlation can occur between U_{10} and T_m^w . It is noted that in the African positions the wind sea heights are slightly higher than swell heights (which decrease in summer) in July (at NA.01) and June (at NA.02). It is also noted that at NA.01 and NA.02 the wind sea and swell heights (and mean periods) are anti-correlated during the year, which is not the case at the Iberian Peninsula positions. At the northernmost two positions, H_s^w only slightly varies during the year (a minor increase occurs at IP.02 during July), leaving swell waves dominating the intra-annual variability of the total SWH. That is not the case at NA.01 and NA.02, where swell dominates the total SWH in winter, but not in spring and summer. At NA.01 from January to May H_s and H_s^s decrease jointly, while H_s^w increase, and after May the total SWH starts to increase jointly with wind sea wave heights, until August/September, while swell wave heights vary very little. A similar situation occurs at

NA.02, although the anti-correlation of H_s^s , and H_s^w cancels the variability of H_s , that is almost constant throughout the year (~2.2 m). The variability of the measured H_s closer to the coast, at buoys G and L, follows the yearly variability in a similar way compared to IP.01, in spite of the distance between the two positions. That is not the case at the S buoy that has two H_s yearly maxima in December and March, and does not follow closely the pattern of intra-annual of variability in position IP.02. The reason for this behavior is due to the sheltering effect of the coast, which does not occur at the northernmost buoys. A completely different situation takes place at buoy G, due to the sheltering effect of the islands, but also due to the distance to key-point NA.01. Here, the intra-annual variability, despite the distance, follows closely the U_{10} and the H_s^w variability pattern of NA.01, since the G position is rather sheltered from remote swell.

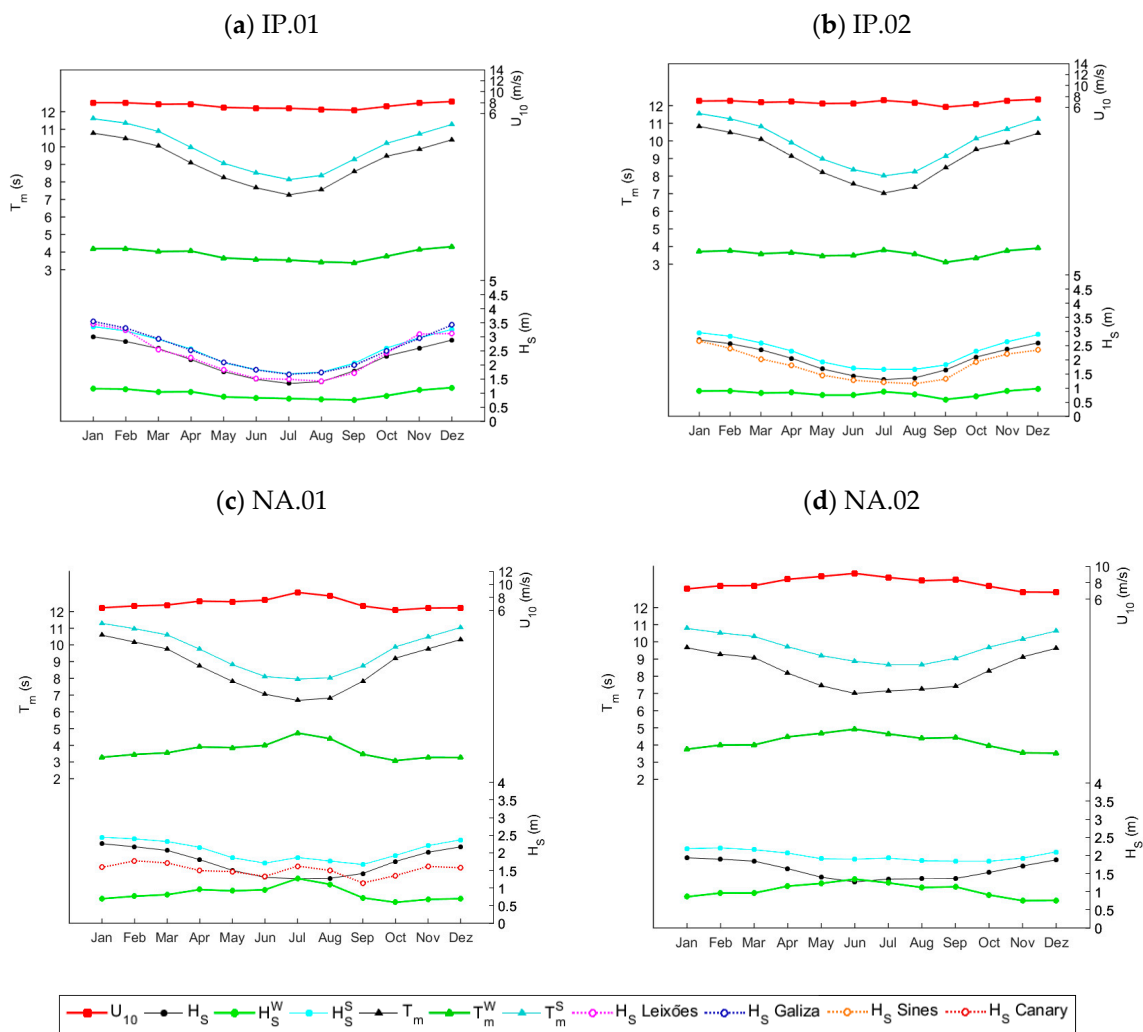


Figure 13. Intra-annual variability of U_{10} ($\text{m}\cdot\text{s}^{-1}$; red line with squares at upper right scale), T_m , T_m^s and T_m^w (s, black, blue and green lines with triangles, respectively, at central left scale), and H_s , H_s^s and H_s^w (m, black, blue and green lines with dots, respectively, at bottom right scale), for key positions (a) IP.01, (b) IP.02, (c) NA.01, and (d) NA.02. The intra-annual variability of the H_s (m) at buoys G and L (blue and magenta dashed lines with open circles) in panel (a), at buoy S (orange dashed line with open circles) panel (b) and at buoy G (red dashed line with open circles) panel (c).

5. Discussion and Conclusions

A detailed study of the wave climate along the EBCCS, based on a qualitative analysis of the wave field, keeping in mind the seasonality of the surface wind speed along the coasts of west

Iberia and north-west Africa, has been presented. The analysis, based on the ECMWF ERA-Interim reanalysis, has been pursued for wind sea and swell waves separately, since SWH and MWP give only a limited description of the sea state, and therefore, a more detailed qualitative investigation is needed to correctly define the wave field characteristics and climate of a certain area. A qualitative knowledge of the wave-field characteristics is needed, mostly because waves play an important role in the modulation of air-sea exchanging, and this modulation is sea-state dependent, i.e., it depends on the type of waves dominating the sea surface. This qualitative analysis is even more necessary when the surface wind speed has a high seasonal variability like along the EBCCS, as shown [51,52]. The ERA-Interim wave heights have been compared to five in situ wave measurements, with good results and, despite its resolution, ERA-Interim has proved to be suited to the regional analysis of the wave field along the EBCCS, in line with what had been previously shown by [37,38], for the analysis of the lower atmosphere winds in the area.

It has been shown that the wind sea and swell characteristics along the EBCCS vary considerably from DJF to JJA, due to the synoptic (in the central North Atlantic sub-basin) and regional (along the coasts of Iberia and north-west Africa) variability of the wind speed. During winter, when the extratropical storms are more frequent and intense, and tracking preferably north-eastward, towards the Norwegian Sea, waves are mostly generated in the central mid- to high latitudinal North Atlantic, propagating as swell towards the Iberian Peninsula and the north-west African coast. In DJF, the wind speed is relatively low along the EBCCS (Figure 3a), particularly along the west coast of Iberia and the coast of north-west Africa, and that explains the low climatological mean H_s^w , compared to H_s^s (Figure 4c,e and Figure 8a), and the high swell predominance (Figure 10a), and high swell energy content (Figure 8a) and power (Figure 8c,e). In summer, the wind sea vs. swell pattern changes, due to the wind speed increase in the area, particularly along the north-west African coast (Figure 3b). This wind speed increase is a regional feature, occurring due to the sharpening of the land-sea temperature (triggered by upwelling), but also due to the interaction of the flow within the MABL with coastal headlands, like Capes Finisterre and Roca, in Iberia, and Capes Cantin and Blanc in Africa. The changes in the regional wind lead to higher climatological H_s^w values in JJA (compared to DJF), which can be comparable to or higher than H_s^s , especially in the lee of Capes Rhir and Blanc (Figure 13). High local wind speed events along the coasts of Morocco and Western Sahara can trigger extreme wind sea heights (~2.5 to 3 m; Figure 5f) in summer, where the wave field is mostly dominated by locally generated waves. These situations can have a strong impact on the atmosphere-wave-ocean coupling (not investigated here), by triggering upwelling events and wave-induced currents, as well as strong wave breaking, whitecapping, sea spray and aerosols dispersion into the atmosphere, that can further be advected into the North Atlantic trades.

The analysis of the SWH and MWP (total, wind sea and swell) intra-annual variability (Figure 13) at four key positions allowed a good assessment of how wind sea and swell waves can combine in the total SWH, proving the need for a more in depth qualitative analysis of the wave field. For example, at key position NA.02 (but to a certain extent also at NA.01), while the monthly mean H_s varies very little during the year, that is not the case with wind sea and swell heights: H_s^s decreases (increases) during summer (winter) months, while H_s^w has an opposite yearly variability, increasing in summer and decreasing in winter.

A more detailed analysis of the effect of local wind speed enhancement by coastal headlands on the wave field along the EBCCA, possibly looking at case studies, should be pursued with higher-resolution wave-model hindcast simulations, taking into account the findings of [85]. Similar studies in other CLLJ areas, where a strong wind speed seasonal variability occurs, as along the Oman CLLJ [70], should also be looked at. During the NAO negative phase, storms can track as far south as northern Morocco, and influence the local wave field in the area. A more detailed analysis of the impact of the large-scale atmospheric circulation, as explained by the NAO index, might also be pursued by looking at case studies through higher-resolution wave-model hindcast simulations and remote-sensing observations. The separate analysis of wind sea and swell allowed also clearer perception of the intrusion of southern

ocean swell waves during JJA (austral winter). A more in-depth analysis of this type of situation, following the method from [86], should also be pursued, with the goal of exploring the meridional migration of the Atlantic Ocean swell front [2]. The cross swell occurrences south of Canary Islands should be investigated, since they can represent sudden changes in MWD and an additional hazard to navigation and maritime operations. Finally, an analysis of the impacts of climate change on the wave field along the EBCCS, following the findings of [71,87–90], is advised as future research.

Acknowledgments: Alvaro Semedo's work was done in the framework of the SOLAR project (PTDC/GEOMET/7078/2014), financed by the Portuguese Foundation for Science and Technology (FCT, *Fundação para a Ciência e Tecnologia*, in Portuguese). Hector Cabrera Bermejo and Gil Lemos are acknowledged for their help with some of the figures.

Conflicts of Interest: The authors declare no conflict of interest.

References

1. Munk, W.H.; Miller, G.R.; Snodgrass, F.E.; Barber, N.F. Directional recording of swell from distant storms. *Philos. Trans. R. Soc. Lond.* **1963**, *A255*, 505–584. [\[CrossRef\]](#)
2. Young, I.R. Seasonal variability of the global ocean wind and wave climate. *Int. J. Climatol.* **1999**, *19*, 931–950. [\[CrossRef\]](#)
3. Alves, J.H. Numerical modeling of ocean swell contributions to the global wind-wave Climate. *Ocean Model.* **2006**, *11*, 98–122. [\[CrossRef\]](#)
4. Ardhuin, F.; Chapron, B.; Collard, F. Observation of swell dissipation across oceans. *Geophys. Res. Lett.* **2009**, *36*, L06607. [\[CrossRef\]](#)
5. Semedo, A.; Sušelj, K.; Rutgersson, A. Variability of Wind Sea and Swell Waves in the North Atlantic Based on ERA-40 Reanalysis. In Proceedings of the 8th European Wave and Tidal Energy Conference 2008, Uppsala, Sweden, 7–10 September 2008.
6. Semedo, A.; Rutgersson, A.; Sterl, A.; Sušelj, K. The global wave age climate. In *Marine Engineering and Technology*; Taylor and Francis Group: London, UK, 2012; pp. 539–543.
7. Semedo, A.; Sušelj, K.; Rutgersson, A.; Sterl, A. A global view on the wind sea and swell climate and variability from ERA-40. *J. Clim.* **2011**, *24*, 1461–1479. [\[CrossRef\]](#)
8. Hanley, K.E.; Belcher, S.E.; Sullivan, P.R. A global climatology of wind-wave interaction. *J. Phys. Oceanogr.* **2010**, *40*, 1263–1282. [\[CrossRef\]](#)
9. Chen, G.; Chapron, B.; Ezraty, R.; Vandemark, D. A global view of swell and wind sea climate in the ocean by satellite altimeter and scatterometer. *J. Atmos. Ocean Technol.* **2001**, *19*, 1849–1859. [\[CrossRef\]](#)
10. Gulev, S.; Grigorieva, V. Variability of the winter wind waves and swell in the North Atlantic and North Pacific as revealed by the voluntary observing ship data. *J. Clim.* **2006**, *19*, 5667–5685. [\[CrossRef\]](#)
11. Jiang, H.; Chen, G. A global view on the swell and wind sea climate by the Jason-1 mission: A revisit. *J. Atmos. Ocean Technol.* **2013**, *30*, 1833–1841. [\[CrossRef\]](#)
12. Carrasco, A.; Semedo, A.; Isachsen, P.E.; Christensen, K.H.; Sætra, Ø. Global surface wave drift climate from ERA-40: The contributions from wind-sea and swell. *Ocean Dyn.* **2014**, *64*, 1815–1829.
13. Rutgersson, A.; Sætra, Ø.; Semedo, A.; Carlson, B.; Kumar, R. Impact of surface waves in a Regional Climate Model. *Meteorol. Z.* **2010**, *19*, 247–257. [\[CrossRef\]](#)
14. Semedo, A.; Sætra, Ø.; Rutgersson, A.; Kahma, K.K.; Pettersson, H. Wave induced wind in the marine boundary layer. *J. Atmos. Sci.* **2009**, *66*, 2256–2271. [\[CrossRef\]](#)
15. Smedman, A.-S.; Höggström, U.; Sahlé, E.; Drennan, W.M.; Kahama, K.K.; Pettersson, H.; Zhang, F. Observational study of marine atmospheric boundary layer characteristics during swell. *J. Atmos. Sci.* **2009**, *66*, 2747–2763. [\[CrossRef\]](#)
16. Höggström, U.; Smedman, A.-S.; Semedo, A.; Rutgersson, A. Comments on “A global climatology of windwave interaction”. *J. Phys. Oceanogr.* **2011**, *41*, 1811–1813. [\[CrossRef\]](#)
17. Höggström, U.; Rutgersson, A.; Sahlé, E.; Smedman, A.-S.; Hristov, T.S.; Drennan, W.M.; Kahma, K.K. Air–Sea interaction features in the Baltic Sea and at a Pacific trade-wind site: An inter-comparison study. *Bound.-Layer Meteorol.* **2013**, *147*, 139–163. [\[CrossRef\]](#)
18. Potter, H. Swell and the drag coefficient. *Ocean Dyn.* **2015**, *65*, 375–384. [\[CrossRef\]](#)

19. Babanin, A.V.; Onorato, M.; Qiao, F. Surface waves and wave-coupled effects in lower atmosphere and upper ocean. *J. Geophys. Res.* **2012**, *117*, C00J01. [[CrossRef](#)]
20. Cavaleri, L.; Fox-Kemper, B.; Hemer, M. Wind waves in the coupled climate system. *Bull. Am. Meteorol. Soc.* **2012**, *93*, 1651–1661. [[CrossRef](#)]
21. Sullivan, P.P.; Edson, J.B.; Hristov, T.; McWilliams, J.C. Large-eddy Simulations and observations of atmospheric marine boundary layers above nonequilibrium surface waves. *J. Atmos. Sci.* **2008**, *65*, 1225–1254. [[CrossRef](#)]
22. Högström, U.; Smedman, A.-S.; Sahlée, E.; Drennan, W.M.; Kahma, K.K.; Johansson, C.; Pettersson, H.; Zhang, F. The atmospheric boundary layer during swell—A field study of the governing mechanism. *J. Atmos. Sci.* **2009**, *66*, 2764–2779. [[CrossRef](#)]
23. Smedman, A.-S.; Högström, U.; Bergström, H.; Rutgersson, A.; Kahma, K.K.; Pettersson, H. A case-study of air-sea interaction during swell conditions. *J. Geophys. Res.* **1999**, *104*, 25833–25851. [[CrossRef](#)]
24. Stokes, G. On the theory of oscillatory waves. *Trans. Camb. Philos. Soc.* **1847**, *8*, 441.
25. McWilliams, J.; Restrepo, J. The wave-driven ocean circulation. *J. Phys. Oceanogr.* **1999**, *29*, 2523–2540. [[CrossRef](#)]
26. Semedo, A.; Vettor, R.; Breivik, Ø.; Sterl, A.; Reistad, M.; Soares, C.G.; Lima, D. The wind sea and swell waves climate in the Nordic seas. *Ocean Dyn.* **2014**, *65*, 223–240. [[CrossRef](#)]
27. Onorato, M.; Waseda, T.; Toffoli, A.; Cavaleri, L.; Gramstad, O.; Janssen, P.A.E.M.; Kinoshita, T.; Monbaliu, J.; Mori, N.; Osborne, A.R.; et al. On the statistical properties of directional ocean waves: The role of the modulational instability in the formation of extreme events. *Phys. Rev. Lett.* **2009**, *102*, 114502. [[CrossRef](#)] [[PubMed](#)]
28. Gordon, H.R.; Jacobs, M.M. Albedo of the ocean-atmosphere system: Influence of sea foam. *Appl. Opt.* **1977**, *16*, 2257–2260. [[CrossRef](#)] [[PubMed](#)]
29. Frouin, R.; Iacobellis, S.F.; Deschamps, P.-Y. Influence of oceanic whitecaps on the global radiation budget. *Geophys. Res. Lett.* **2001**, *28*, 1523–1526. [[CrossRef](#)]
30. Holthuijse, L.H. *Waves in Oceanic and Coastal Waters*; Cambridge University Press: Cambridge, UK, 2008; p. 387.
31. Gerling, T.W. Partitioning sequences and arrays of directional wave spectra into component wave systems. *J. Atmos. Ocean. Technol.* **1992**, *9*, 444–458. [[CrossRef](#)]
32. Hanson, J.L.; Phillips, O.M. Automated analysis of ocean surface directional wave spectra. *J. Atmos. Ocean. Technol.* **2001**, *18*, 277–293. [[CrossRef](#)]
33. Kumar, N.; Cahl, D.L.; Crosby, S.C.; Voulgaris, G. Bulk versus spectral wave parameters: Implications on stokes drift estimates, regional wave modeling, and HF radars applications. *J. Phys. Oceanogr.* **2017**, *43*, 1413–1431. [[CrossRef](#)]
34. Hegermiller, C.A.; Rueda, A.; Erikson, L.H.; Barnard, P.L.; Antolinez, J.A.A.; Mendez, F.J. Controls of multimodal wave conditions in a complex coastal setting. *Geophys. Res. Lett.* **2017**, *44*, 12315–12323. [[CrossRef](#)]
35. Young, I.R.; Zieger, S.; Babanin, A.V. Global Trends in Wind Speed and Wave Height. *Science* **2011**, *332*, 451–455. [[CrossRef](#)] [[PubMed](#)]
36. Pandian, P.K.; Emmanuel, O.; Ruscoe, J.P.; Side, J.C.; Harris, R.E.; Kerr, S.A.; Bullen, C.R. An overview of recent technologies on wave and current measurement in coastal and marine applications. *J. Oceanogr. Mar. Sci.* **2011**, *1*, 001–010.
37. Sterl, A. On the (in-)homogeneity of reanalysis products. *J. Clim.* **2004**, *17*, 3866–3873. [[CrossRef](#)]
38. Aarnes, O.J.; Abdalla, S.; Bidlot, J.-R.; Breivik, Ø. Marine Wind and Wave Height Trends at Different ERA-Interim Forecast Ranges. *J. Clim.* **2015**, *28*, 819–837. [[CrossRef](#)]
39. Ranjha, R.; Svensson, G.; Tjernström, M.; Semedo, A. Global distribution and seasonal variability of coastal low-level jets derived from ERA-Interim reanalysis. *Tellus A* **2013**, *65*, 20412. [[CrossRef](#)]
40. Lima, D.C.A.; Soares, P.M.M.; Cardoso, C.R.; Semedo, A. A Global View of Coastal Low-Level Wind Jets using an Ensemble of Reanalysis. *J. Clim.* **2018**, *4*, 1525–1546. [[CrossRef](#)]
41. Winant, C.D.; Dorman, C.E.; Friehe, C.A.; Beardsley, R.C. The marine layer off northern California: An example of supercritical channel flow. *J. Atmos. Sci.* **1988**, *45*, 3588–3605. [[CrossRef](#)]
42. Vallis, G.K. Large-scale Circulation and Production of Stratification: Effects of Wind, Geometry and Diffusion. *J. Phys. Oceanogr.* **2000**, *30*, 933–954. [[CrossRef](#)]

43. Barton, E.D.; Field, D.B.; Roy, C. Canary current upwelling: More or less? *Prog. Oceanogr.* **2013**, *116*, 167–178. [[CrossRef](#)]
44. Tuomi, L.; Kahma, K.K.; Pettersson, K. Wave hindcast statistics in the seasonally ice covered Baltic Sea. *Boreal Environ. Res.* **2011**, *16*, 451–472.
45. Galanis, G.; Hayes, D.; Zodiatis, G.; Chu, P.C.; Kuo, Y.-H.; Kallos, G. Wave height characteristics in the Mediterranean Sea by means of numerical modeling, satellite data, statistical and geometrical techniques. *Mar. Geophys. Res.* **2015**, *33*, 55–76. [[CrossRef](#)]
46. Beardsley, R.C.; Dorman, C.E.; Friehe, C.A.; Rosenfield, L.K.; Wyant, C.D. Local atmospheric forcing during the Coastal Ocean Dynamics Experiment 1: A description of the marine boundary layer and atmospheric conditions over a northern California upwelling region. *J. Geophys. Res.* **1987**, *92*, 1467–1488. [[CrossRef](#)]
47. Bakun, A. Global Climate Change and Intensification of Coastal Ocean Upwelling. *Science* **1990**, *247*, 198–201. [[CrossRef](#)] [[PubMed](#)]
48. Small, C.; Nicholls, R.J. A global analysis of human settlement in coastal zones. *J. Coast. Res.* **2003**, *19*, 584–599.
49. Narayan, N.; Paul, A.; Mulitza, S.; Schulz, M. Trends in Coastal Upwelling Intensity. *Ocean Sci.* **2010**, *6*, 815–823. [[CrossRef](#)]
50. Miranda, P.M.A.; Alves, J.M.R.; Serra, N. Climate Change and Upwelling: Response of Iberian Upwelling to Atmospheric Forcing in a Regional Climate Scenario. *Clim. Dyn.* **2013**, *40*, 2813–2824. [[CrossRef](#)]
51. Montagne, R.; de la Prédiction, L.S.; de la Houle, M. *Annales Hydrographiques*; Imprimerie Nationale: Paris, France, 1922; pp. 157–186.
52. Mekadem, N.E.; Moutchou, M.E.B.E.; Bernabeu, A.M.; Hajjaji, K.E. Grain Size Analysis and Wave Modeling on the Coastal. *J. Shipp. Ocean Eng.* **2012**, *2*, 244–248.
53. Soares, P.M.M.; Cardoso, R.; Semedo, A.; Chinita, M.J.; Ranjha, R. The Iberian Peninsula Coastal Low Level Jet. *Tellus A* **2014**, *66*, 22377. [[CrossRef](#)]
54. Rijo, N.; Semedo, A.; Miranda, P.M.A.; Lima, D.C.A.; Cardoso, R.M.; Soares, P.M.M. Spatial and Temporal Variability of the Iberian Peninsula Coastal Low-Level Jet. *Int. J. Climatol.* **2017**, *38*, 1605–1622. [[CrossRef](#)]
55. Dee, D.P.; Uppala, S.M.; Simmons, A.J.; Berrisford, P.; Poli, P.; Kobayashi, S.; Andrae, U.; Balmaseda, M.A.; Balsamo, G.; Bauer, P.; et al. The ERA-Interim Reanalysis: Configuration and Performance of the Data Assimilation System. *Q. J. R. Meteorol. Soc.* **2011**, *137*, 553–597. [[CrossRef](#)]
56. Janssen, P.A.E.M. *The Interaction of Ocean Waves and Wind*; Cambridge University Press: Cambridge, UK, 2004; p. 300.
57. WAMDI Group. The WAM model—A third generation oceanwave prediction model. *J. Phys. Oceanogr.* **1988**, *18*, 1775–1810.
58. Dee, D.P.; Uppala, S. Variational bias correction of satellite radiance data in the ERA-Interim reanalysis. *Q. J. R. Meteorol. Soc.* **2009**, *135*, 1830–1841. [[CrossRef](#)]
59. Stopa, J.; Cheung, K.F. Intercomparison of wind and wave data from the ECMWF Reanalysis Interim and the NCEP Climate Forecast System Reanalysis. *Ocean Model.* **2014**, *75*, 65–83. [[CrossRef](#)]
60. Pierson, W.J.; Moskowitz, L. A proposed spectral form for fully developed wind seas based on the similarity theory of S.A. Kitaigorodskii. *J. Geophys. Res.* **1964**, *69*, 5181–5190. [[CrossRef](#)]
61. Alves, J.H.; Banner, M.L.; Young, I.R. Revisiting the Pierson-Moskowitz asymptotic limits for fully developed wind waves. *J. Phys. Oceanogr.* **2003**, *33*, 1301–1323. [[CrossRef](#)]
62. Bidlot, J.-R. *ECMWF Wave Model Products*; ECMWF Newsletter, No. 91; ECMWF: Reading, UK, 2001; pp. 9–15.
63. Sterl, A.; Caires, S. Climatology, variability and extrema of ocean waves: The Web-based KNMI/ERA-40 wave atlas. *Int. J. Climatol.* **2005**, *25*, 963–997. [[CrossRef](#)]
64. Holt, T.R. Mesoscale forcing of a boundary layer jet along the California coast. *J. Geophys. Res.* **1996**, *101*, 4235–4254. [[CrossRef](#)]
65. Parish, T.R. Forcing of the summertime low-level jet along the California coast. *J. Appl. Meteorol.* **2000**, *39*, 2421–2433. [[CrossRef](#)]
66. Jiang, Q.; Wang, S.; O’Neill, L. Some insights into the characteristics and dynamics of the Chilean Low-Level Coastal Jet. *Mon. Weather Rev.* **2010**, *138*, 3185–3206. [[CrossRef](#)]
67. Nicholson, S.E. A low-level jet along the Benguela coast, an integral part of the Benguela current ecosystem. *Clim. Chang.* **2010**, *99*, 613–624. [[CrossRef](#)]

68. Burk, S.D.W.T. Thompson, The summertime low-level jet and marine boundary layer structure along the California coast. *Mon. Weather Rev.* **1996**, *124*, 668–686. [[CrossRef](#)]
69. Zemba, J.; Friehe, C.A. The marine boundary layer jet in the coastal ocean dynamics experiment. *J. Geophys. Res.* **1987**, *92*, 1489–1496. [[CrossRef](#)]
70. Ranjha, R.; Tjernström, M.; Semedo, A.; Svensson, G.; Cardoso, R.M. Structure and Variability of the Oman Coastal Low-Level Jet. *Tellus A* **2015**, *67*, 25285. [[CrossRef](#)]
71. Semedo, A.; Soares, P.M.M.; Lima, D.C.A.; Cardoso, R.M.; Bernardino, M.; Miranda, P.M.A. The impact of Climate Change on the Global Coastal Low-Level Wind Jets: EC-EARTH simulations. *Glob. Planet. Chang.* **2016**, *137*, 88–106. [[CrossRef](#)]
72. Rijo, N.; Lima, D.C.A.; Semedo, A.; Miranda, P.M.A.; Cardoso, R. The Iberian Peninsula low-level coastal jet: Climatology and case study analysis. In Proceedings of the 10th Jornadas do Mar 2014, Lisbon, Portugal, 11–14 November 2014.
73. Tjernström, M.; Grisogono, B. Simulations of supercritical flow around points and capes in the coastal atmosphere. *J. Atmos. Sci.* **2000**, *57*, 108135. [[CrossRef](#)]
74. Hurrell, J.W. Influence of variations in extratropical wintertime teleconnections on Northern Hemisphere temperature. *Geophys. Res. Lett.* **1996**, *23*, 665–668. [[CrossRef](#)]
75. Luo, D.; Diao, Y.; Feldstein, S.B. The variability of the atlantic storm track and the North Atlantic Oscillation: A link between intraseasonal and interannual variability. *J. Atmos. Sci.* **2011**, *68*, 577–601. [[CrossRef](#)]
76. Semedo, A. The North Atlantic Oscillation Influence on the Wave Regime in Portugal: An Extreme Event Analysis. Master's Thesis, Meteorology Naval Postgraduate School, Monterey, CA, USA, 2005.
77. Sempreviva, A.M.; Schiano, M.E.; Pensieri, S.; Bozzano, R.; Borghini, M.; Grasso, F.; Semedo, A.; Soerensen, L.-L.; Teixeira, J.; Tranter, C.; et al. Observed development of the vertical structure of the marine boundary layer during the LASIE experiment in the Ligurian Sea. *Ann. Geophys.* **2010**, *28*, 17–25. [[CrossRef](#)]
78. Peliz, A.; Dubert, J.; Marchesiello, P.; Teles-Machado, A. Surface circulation in the Gulf of Cadiz: Model and mean flow structure. *J. Geophys. Res.* **2007**, *112*, C11015. [[CrossRef](#)]
79. Reguero, B.G.; Losada, I.J.; Méndez, F.J. A global wave power resource and its seasonal, interannual and long-term variability. *Appl. Energy* **2015**, *148*, 366–380. [[CrossRef](#)]
80. Bromirski, P.D.; Cayan, D.R. Wave power variability and trends across the North Atlantic influenced by decadal climate patterns. *J. Geophys. Res.* **2015**, *120*, 3419–3443. [[CrossRef](#)]
81. Jeffreys, H. On the formation of waves by wind. *Proc. R. Soc.* **1924**, *A107*, 189–206.
82. Jeffreys, H. On the formation of waves by wind. II. *Proc. R. Soc.* **1925**, *A110*, 341–347.
83. Smith, S.D.; Anderson, R.J.; Oost, W.A. Coauthors Sea surface wind stress and drag coefficients: The HEXOS results. *Bound.-Layer Meteorol.* **1992**, *60*, 109–142. [[CrossRef](#)]
84. Rijo, N.; Semedo, A.; Lima, D.C.A.; Miranda, P.M.A.; Cardoso, R.; Soares, P.M.M. The Northerly Summer Wind off the West Coast of the Iberian Peninsula. In Proceedings of the TransNav 2015—International Conference on Marine Navigation and Safety of Sea Transportation, Gdynia, Poland, 17–19 June 2015.
85. Ranjha, R.; Tjernström, M.; Svensson, G.; Semedo, A. Modeling Coastal Low-Level Wind-Jets: Does horizontal resolution matter? *Met. Atmos. Phys.* **2015**, *128*, 263–278. [[CrossRef](#)]
86. Ardhuin, F.; Jenkins, A. On the Interaction of surface waves and upper ocean turbulence. *J. Phys. Oceanogr.* **2006**, *33*, 551–557. [[CrossRef](#)]
87. Semedo, A.; Weisse, R.; Beherens, A.; Sterl, A.; Bengtsson, L.; Gunther, H. Projection of global wave climate change towards the end of the 21st century. *J. Clim.* **2013**, *26*, 8269–8288. [[CrossRef](#)]
88. Cardoso, R.M.; Soares, P.M.M.; Lima, D.C.A.; Semedo, A. The impact of Climate Change on the Iberian Low-Level Wind Jet: EURO-CORDEX—Regional climate simulation. *Tellus* **2015**, *68*, 29005. [[CrossRef](#)]
89. Soares, P.M.M.; Lima, D.C.A.; Cardoso, R.M.; Semedo, A. High resolution projections for the western Iberian coastal low level jet in a changing climate. *Clim. Dyn.* **2017**, *49*, 1547. [[CrossRef](#)]
90. Soares, P.M.M.; Lima, D.C.A.; Cardoso, R.M.; Nascimento, M.L.; Semedo, A. Western iberian offshore wind resources: More or less in a global warming climate? *Appl. Energy* **2017**, *203*, 72–90. [[CrossRef](#)]

